Early American settlers

This file contains 4 documents:

(1) **Archaeologists uncover oldest known projectile points in the Americas** January 5, 2023

Source: https://www.sciencedaily.com/releases/2022/12/221226094527.htm

(2) **Dating of a large tool assemblage at the Cooper's Ferry site (Idaho, USA) to ~15,785 cal yr B.P. extends the age of stemmed points in the Americas** Dec 23, 2022

Source: https://www.science.org/doi/10.1126/sciadv.ade1248

(3) **Bering Land Bridge formed surprisingly late during last ice age** Dec 26, 2022

Source: https://www.sciencedaily.com/releases/2022/12/221226151545.htm

(4) **The Bering Strait was flooded 10,000 years before the Last Glacial Maximum** Dec 27, 2022

Source: https://www.pnas.org/doi/10.1073/pnas.2206742119

[Assembled by Wergosum on 2023-01-06. Downloadable from https://wergosum.com/wp-content/uploads/2023/01/20230106_Early American settlers.pdf]

ScienceDaily®
Your source for the latest research news

Archaeologists uncover oldest known projectile points in the Americas

Date: December 26, 2022

Source: Oregon State University

Summary: Archaeologists have uncovered projectile points in Idaho that are thousands of years older than any previously found in the Americas, helping to fill in the history of how early humans crafted and used stone weapons.

FULL STORY

Oregon State University archaeologists have uncovered projectile points in Idaho that are thousands of years older than any previously found in the Americas, helping to fill in the history of how early humans crafted and used stone weapons.

The 13 full and fragmentary projectile points, razor sharp and ranging from about half an inch to 2 inches long, are from roughly 15,700 years ago, according to carbon-14 dating. That's about 3,000 years older than the Clovis fluted points found throughout North America, and 2,300 years older than the points previously found at the same Cooper's Ferry site along the Salmon River in present-day Idaho.

The findings were published today in the journal *Science Advances.*

"From a scientific point of view, these discoveries add very important details about what the archaeological record of the earliest peoples of the Americas looks like," said Loren Davis, an anthropology professor at OSU and head of the group that found the points. "It's one thing to say, 'We think that people were here in the Americas 16,000 years ago;' it's another thing to measure it by finding well-made artifacts they left behind."

Previously, Davis and other researchers working the Cooper's Ferry site had found simple flakes and pieces of bone that indicated human presence about 16,000 years ago. But the discovery of projectile points reveals new insights into the way the first Americans expressed complex thoughts through technology at that time, Davis said.

The Salmon River site where the points were found is on traditional Nez Perce land, known to the tribe as the ancient village of Nipéhe. The land is currently held in public ownership by the federal Bureau of Land Management.

The points are revelatory not just in their age, but in their similarity to projectile points found in Hokkaido, Japan, dating to 16,000-20,000 years ago, Davis said. Their presence in Idaho adds more detail to the hypothesis that there are early genetic and cultural connections between the ice age peoples of Northeast Asia and North America.

"The earliest peoples of North America possessed cultural knowledge that they used to survive and thrive over time. Some of this knowledge can be seen in the way people made stone tools, such as the projectile points found at the Cooper's Ferry site," Davis said. "By comparing these points with other sites of the same age and older, we can infer the spatial extents of social networks where this technological knowledge was shared between peoples."

These slender projectile points are characterized by two distinct ends, one sharpened and one stemmed, as well as a symmetrical beveled shape if looked at head-on. They were likely attached to darts, rather than arrows or spears, and despite the small size, they were deadly weapons, Davis said.

"There's an assumption that early projectile points had to be big to kill large game; however, smaller projectile points mounted on darts will penetrate deeply and cause tremendous internal damage," he said. "You can hunt any animal we know about with weapons like these."

These discoveries add to the emerging picture of early human life in the Pacific Northwest, Davis said. "Finding a site where people made pits and stored complete and broken projectile points nearly 16,000 years ago gives us valuable details about the lives of our region's earliest inhabitants."

The newly discovered pits are part of the larger Cooper's Ferry record, where Davis and colleagues have previously reported a 14,200-year-old fire pit and a food-processing area containing the remains of an extinct horse. All told, they found and mapped more than 65,000 items, recording their locations to the millimeter for precise documentation.

The projectile points were uncovered over multiple summers between 2012 and 2017, with work supported by a funding partnership held between OSU and the BLM. All excavation work has been completed and the site is now covered. The BLM installed interpretive panels and a kiosk at the site to describe the work.

Davis has been studying the Cooper's Ferry site since the 1990s when he was an archaeologist with the BLM. Now, he partners with the BLM to bring undergraduate and graduate students from OSU to work the site in the summer. The team also works closely with the Nez Perce tribe to provide field opportunities for tribal youth and to communicate all findings.

Story Source:

Materials provided by **Oregon State University**. Original written by Molly Rosbach. *Note: Content may be edited for style and length.*

Related Multimedia:

- Excavations and the arrow tips

Journal Reference:

1. Loren G. Davis, David B. Madsen, David A. Sisson, Lorena Valdivia-Becerra, Thomas Higham, Daniel Stueber, Daniel W. Bean, Alexander J. Nyers, Amanda Carroll, Christina Ryder, Matt Sponheimer, Masami Izuho, Fumie Iizuka, Guoqiang Li, Clinton W. Epps, F. Kirk Halford. **Dating of a large tool assemblage at the Cooper's Ferry site (Idaho, USA) to ~15,785 cal yr B.P. extends the age of stemmed points in the Americas**. *Science Advances*, 2022; 8 (51) DOI: 10.1126/sciadv.ade1248

Cite This Page:

MLA | APA | Chicago

Oregon State University. "Archaeologists uncover oldest known projectile points in the Americas." ScienceDaily. ScienceDaily, 26 December 2022. <www.sciencedaily.com/releases/2022/12/221226094527.htm>.

ANTHROPOLOGY

Dating of a large tool assemblage at the Cooper's Ferry site (Idaho, USA) to ~15,785 cal yr B.P. extends the age of stemmed points in the Americas

Loren G. Davis[1]*, David B. Madsen[2], David A. Sisson[3], Lorena Valdivia-Becerra[4], Thomas Higham[5,6], Daniel Stueber[7], Daniel W. Bean[1], Alexander J. Nyers[1,8], Amanda Carroll[9], Christina Ryder[10], Matt Sponheimer[10], Masami Izuho[11], Fumie Iizuka[12], Guoqiang Li[13], Clinton W. Epps[14], F. Kirk Halford[15]

The timing and character of the Pleistocene peopling of the Americas are measured by the discovery of unequivocal artifacts from well-dated contexts. We report the discovery of a well-dated artifact assemblage containing 14 stemmed projectile points from the Cooper's Ferry site in western North America, dating to ~16,000 years ago. These stemmed points are several thousand years older than Clovis fluted points (~13,000 cal yr B.P.) and are ~2300 years older than stemmed points found previously at the site. These points date to the end of Marine Isotope Stage 2 when glaciers had closed off an interior land route into the Americas. This assemblage includes an array of stemmed projectile points that resemble pre-Jomon Late Upper Paleolithic tools from the northwestern Pacific Rim dating to ~20,000 to 19,000 years ago, leading us to hypothesize that some of the first technological traditions in the Americas may have originated in the region.

INTRODUCTION

Archaeological excavations in Area A at the Cooper's Ferry site, located on a terrace of the lower Salmon River of western Idaho (Fig. 1), produced a record of a ~16,000- to 13,200-year-old stone tool assemblage that included the earliest known stemmed points in western North America (*1*). This evidence was found in a deeply buried layer of pedogenically altered glacial loess, termed lithostratigraphic unit 3 (LU3) (Fig. 2). LU3 contains a paleosol, called the Rock Creek Soil, which includes a rubified A horizon, calcic B horizon, and loessal C horizon formed roughly in the middle of the 75- to 50-cm-thick LU3 loess deposits in Area A. The Rock Creek Soil has been dated between ~16,450 and 14,160 calibrated years before the present (cal yr B.P.) at multiple localities in the lower Salmon River canyon upstream of the site (*2*–*4*). An erosional unconformity at the top of the unit removed an unknown amount of the LU3 loess and deposits immediately overlying LU3. Four cultural features were found in LU3, including three pits that contained a tooth fragment from an extinct *Equus* sp., numerous bone fragments, flake tools, debitage, and a hearth feature with charcoal radiocarbon dated to ~14,660 cal yr B.P. (Fig. 2: F142, F144, F143, and F129). Radiocarbon dating of culturally associated animal bone and charcoal from the middle portion of LU3 returned ages between ~15,660 and 14,650 cal yr B.P., while Bayesian modeling predicted that LU3 sediment deposition and initial human occupation in Area A began sometime between 16,560 and 15,280 cal yr B.P. [95.4% confidence interval (CI)]. However, while in situ flake tools, debitage, a fire cracked rock(FCR), animal bone fragments, and small pieces of charcoal were also recovered stratigraphically in the lower half of LU3 below the pits and hearth, no formal stone tools, cultural features, or radiocarbon dated samples were recovered from the deeper LU3 sediments, forcing us to rely on Bayesian modeling to estimate that the initial occupation at the site began sometime ~16,000 cal yr B.P. The use of this statistical modeling, together with the limited artifact array from the lowest LU3 loess, has led to some speculation that the artifacts in lower LU3 were present because of stratigraphic mixing and that the site's earliest cultural remains were not as old as hypothesized (*5*, *6*).

Now, we can report the results of separate excavations conducted at the site's eastern side in Area B, which revealed additional contemporaneous evidence of early cultural occupation at the site and helps confirm the early age estimates derived from the Area A excavations. We report consistent ^{14}C ages from excavated cultural pits originating wholly within the lowest cultural deposits in Area B ranging from 13,260 ± 240 to 13,091 ± 48 yr B.P. (16,675 to 15,240 cal yr B.P. to 15,772 to 15,617 cal yr B.P.). These formal cultural features and the surrounding sediments contain 14 complete and fragmentary stemmed projectile points, other stone tools, substantial amounts of lithic debris, and animal bone fragments. The found projectile points are thousands of years older than Clovis

[1]Department of Anthropology, Oregon State University, 203 Waldo Hall, Corvallis, OR 97331, USA. [2]Department of Anthropology, University of Nevada-Reno, 512 Ansari, Reno, NV 89557, USA. [3]Bureau of Land Management, Cottonwood Field Office, 2 Butte Drive, Cottonwood, ID 83522, USA. [4]Oxford Radiocarbon Accelerator Unit, School of Archaeology, 1 South Parks Road, Oxford OX1 3TG, UK. [5]Department of Evolutionary Anthropology, University of Vienna, Djerassiplatz 1, 1030 Wien, Austria. [6]Human Evolution and Archaeological Sciences (HEAS), University of Vienna, A-1030 Vienna, Austria. [7]Department of Anthropology, University of Victoria, P.O. Box 1700 STN CSC, Victoria, BC V8W 2Y2, Canada. [8]Northwest Archaeometrics, 5060 SW Philomath Blvd, #331, Corvallis, OR 97333, USA. [9]SWCA Environmental Consultants, 1800 NW Upshur St, Ste. 100, Portland, OR 97209, USA. [10]Department of Anthropology, University of Colorado Boulder, Hale Science Building, 1350 Pleasant St., Boulder, CO 80309, USA. [11]Tokyo Metropolitan University, Faculty of Humanities and Social Sciences, 1-1 Minami-Osawa, Hachioji-shi, Tokyo 192-0397, Japan. [12]Department of Anthropology and Research Reactor Center, University of Missouri, Swallow Hall, 112 S 9th Street, Columbia, MO 65211, USA. [13]Research School of Arid Environment and Climate Change, MOE Key Laboratory of West China's Environmental System, Lanzhou University, 222 Tianshuinanlu, Lanzhou, Gansu 730000, China. [14]Oregon State University Department of Fisheries, Wildlife, and Conservation Sciences, 104 Nash Hall, Corvallis, OR 97331, USA. [15]Department of Anthropology, Boise State University, Boise, ID 83725, USA.
*Corresponding author. Email: loren.davis@oregonstate.edu

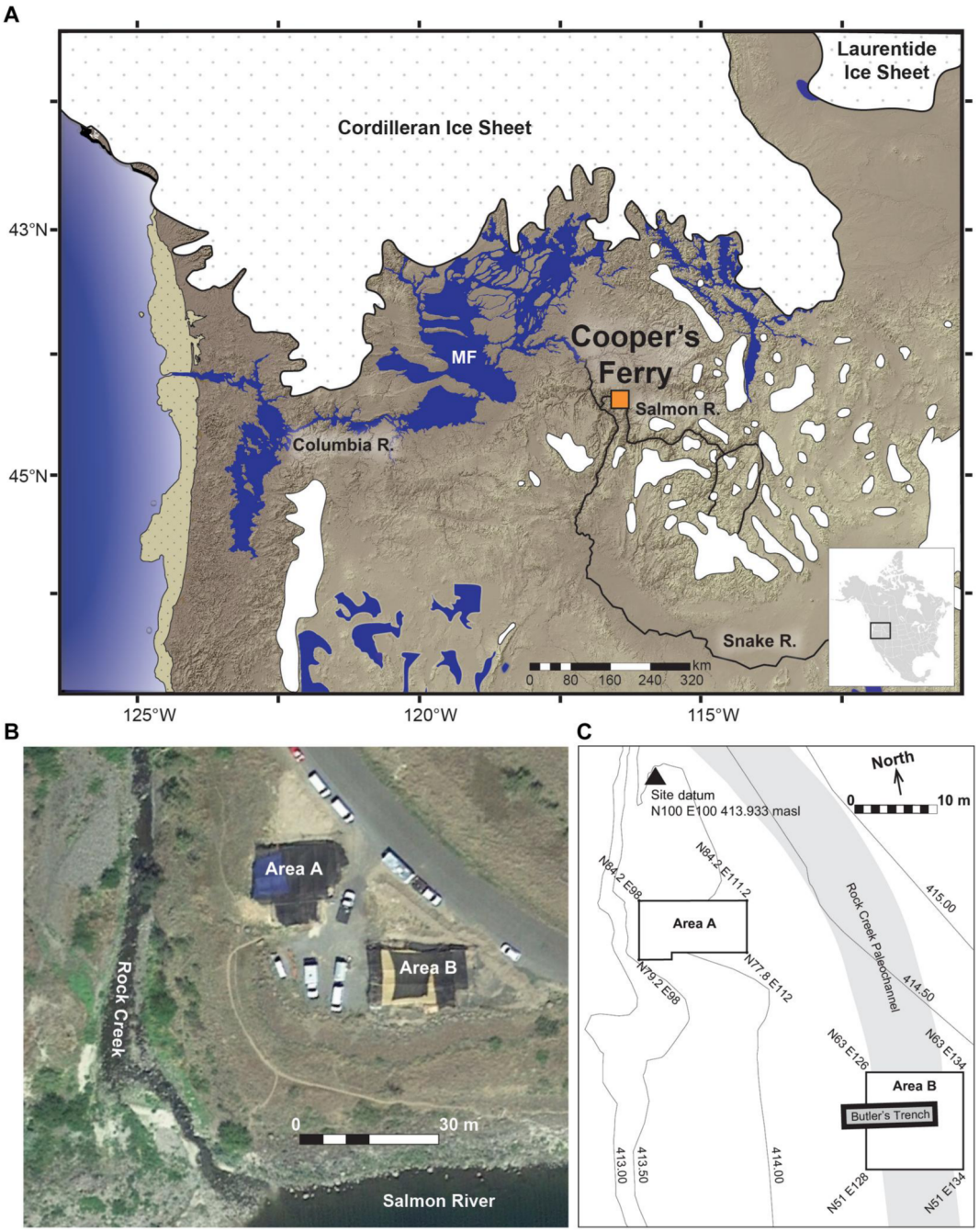

Fig. 1. Location maps and aerial images showing the location of the Cooper's Ferry site and excavation areas. Paleoenvironmental conditions in the Pacific Northwest during glacial conditions at ~16,000 calibrated years before the present (cal yr B.P.) shown in (**A**). Aerial image of the site showing the location of Area A and Area B in relation to the Salmon River (**B**). Site map showing the location of Butler's Trench and the Rock Creek Paleochannel (**C**). Projected regional environmental aspects at ~16,000 cal yr B.P. are based on modeled extents of Cordilleran and Laurentide glacial ice (*31*), mountain glacier complexes (*32*), positions of Glacial Lake Missoula, Glacial Lake Columbia, the modeled path of the Missoula Flood (MF) and its impoundment pool (*33*), smaller northern Great Basin pluvial lakes (*34*), and shoreline extents along the Pacific outer continental shelf (shown as a tan dotted area at left) (*35*). Aerial image shown in (B) shows excavations in progress on 30 July 2016 (*36*). masl, m above sea level.

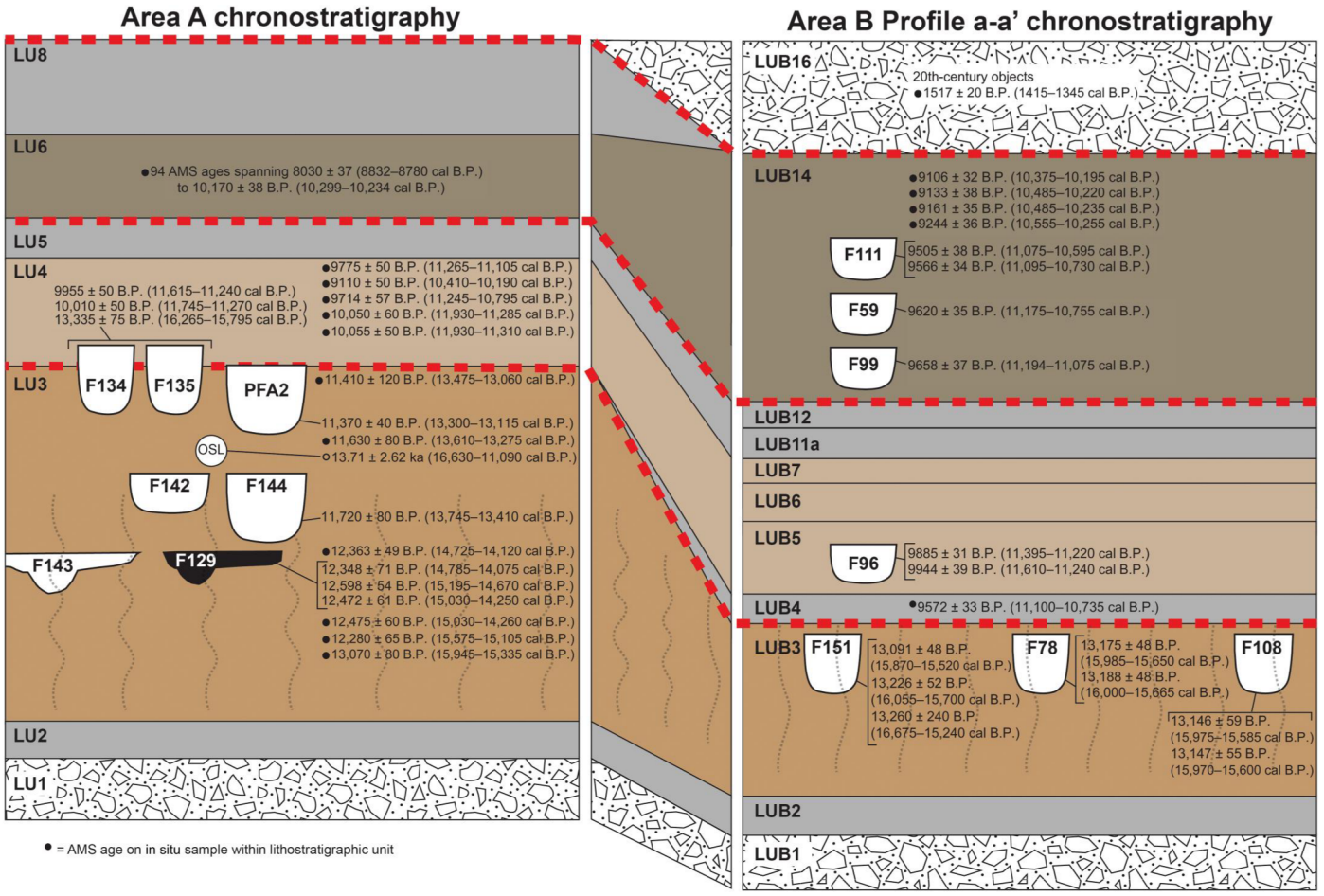

Fig. 2. Chronostratigraphic correlation between Area A and Area B. Dashed lines indicate erosional surfaces. Wavy lines show areas of soil development. Black circles indicate radiocarbon ages from samples recovered in a stratigraphic unit. Radiocarbon ages without circles are from cultural features. Radiocarbon ages on LU3 samples derived from rodent burrows (*1*) are not shown. The vertical scale of each composite stratigraphic profile is ~3.0 m. OSL, optically stimulated luminescence. AMS- accelerator mass spectrometry.

fluted points (~13,000 cal yr B.P.) in North America (*7*, *8*) and are ~2300 years older than stemmed points previously found in Area A (*1*). This evidence greatly extends the timing of stemmed point technology in the Americas. Moreover, unlike several other pre-Clovis age sites in North America (*8*), the tool assemblage from lower LU3 is now quite large, allowing its morphological/technological characteristics to be determined and used in a search for where the antecedents of that technological tradition may be found. We hypothesize that the form of these early stemmed points and the lithic technology used to produce them are similar to bifacial points found in northeast Asia, particularly northern Japan, dating to the Late Upper Paleolithic ~21,400 to 16,170 cal yr B.P. (*9*). Here, we describe the Area B stratigraphy and chronology, characterize this early Cooper's Ferry stemmed point assemblage, and discuss its implications for understanding the Pleistocene archaeology of the Americas.

RESULTS

Archaeological excavations were conducted at the Cooper's Ferry site from 2012 to 2018 at a location designated as Area B (Fig. 1 and fig. S1). The base of these excavations exposed a stratified sequence of alluvial gravel and sand deposits (LUB1-LUB2) overlain by loess (LUB3; Figs. 2 and 3 and fig. S2). These LUs are informally designated at the site level. A backhoe trench used to test the sediments in Area B in the 1960s (*10*) partially disturbed some of the deposits in Area B, but given the readily identifiable intact sediments of the LUB3 brown loess, these darker disturbed trench deposits were easily recognized and discarded before excavation.

Area B stratigraphy

Area B is located closer to both the Salmon River and a paleochannel of the nearby Rock Creek (Fig. 1). As a result, its upper stratigraphy is more complex than that in the adjacent Area A (*1*) because of slightly different erosional and depositional factors related to this proximity. However, the lowest sedimentary units containing the earliest cultural deposits can be readily traced across the site to Area A (Fig. 2). The stratigraphy of Area B includes 11 LUs and an occurrence of the Rock Creek Soil (Figs. 2 and 3 and table S1). LUB3, the equivalent of LU3 in Area A, is a loess that overlies the LUB2 and LUB1 alluvium. The same erosional unconformity at the top of LU3 also occurs at the top of LUB3, but more of the upper

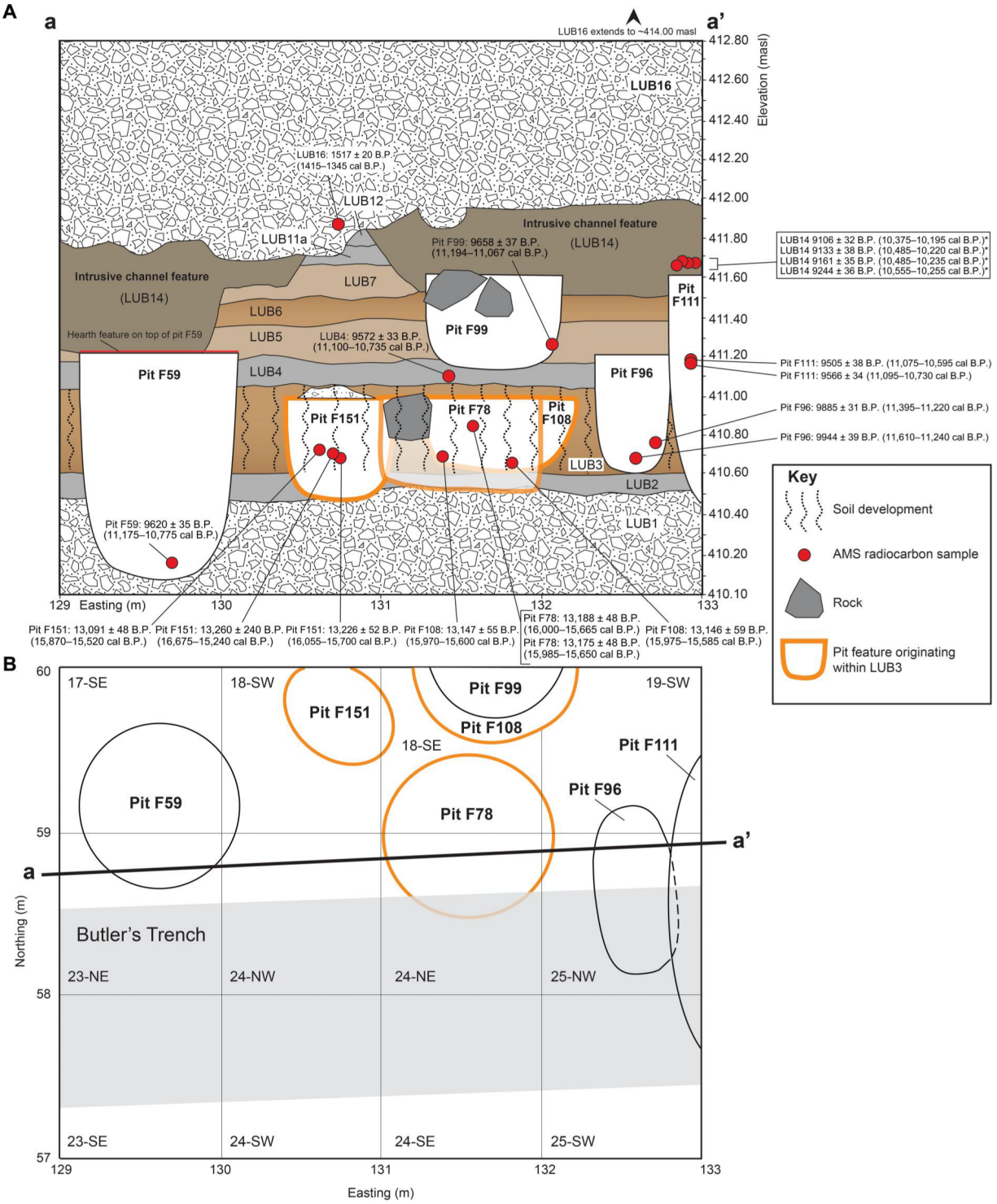

Fig. 3. Composite stratigraphy of Area B. Drawing of stratigraphic units exposed along the a-a′ easting profile (**A**). Looking north into the deposits arranged near the a-a′ stratigraphic transect–pits F151 and F108 are positioned behind pit F78. To show this arrangement, the fill of F78 is made partially transparent. Plan view of Area B's deepest excavation units showing distribution of pit features and trench excavation placed by Butler (**B**). Excavation unit numbers and quadrant designations are shown in each 1 m–by–1 m square (e.g., 23-SE).

loess deposits of this sedimentary unit were removed in Area B than in Area A. As a result, only the lower portion of the LU3 loess–equivalent sediments remains in LUB3.

This erosion also removed the upper portion of the Rock Creek Soil in Area B, and only the calcic B and loessal C horizons remain. This paleosol formed after the construction of the cultural pit features described below as the carbonate horizon extends through the fill of these pits. Bone fragments and stone artifacts in LUB3, including those in the pits, bear heavy carbonate coatings associated with Rock Creek Soil pedogenesis (fig. S3). This carbonate coating distinguishes LUB3 artifacts from the artifacts found in the overlying sediments and indicates that their deposition at the site predates the 16,450 to 14,160 cal yr B.P. formation of the Rock Creek Soil (*2*–*4*, see the supplementary materials).

Archaeological evidence originating within LUB3

Layer LUB3 contained three cylindrical cultural pit features designated as F78, F108, and F151 (Fig. 2 and figs. S4 to S9). Feature 78 (~105 cm in diameter and ~50 cm deep) contained four complete and fragmentary stemmed projectile points (Fig. 4), a small fragment of what appears to be a stemmed point base, a fragment of a biface, a burin spall, a small edge fragment of a core, 250 pieces of debitage, seven pieces of FCR, two pieces of charcoal, and 226 fragments of animal bone (tables S2 and S3). The top of the F78 pit lies below the upper limits of LUB3, as marked by a clear stratigraphic boundary of contrasting pit fill sediments and a large angular basalt cobble, the top of which was buried by the continued deposition of LUB3 loess (fig. S4). Pit F108 (~90 cm in diameter and ~40 cm deep) is positioned immediately north of and at the same elevation as pit F78, as revealed by the presence of artifacts and faunal materials in a carbonate-rich pit fill (figs. S7 and S10). Feature 108 contained seven complete and fragmentary stemmed projectile points (Fig. 4), 53 pieces of debitage, and 21 fragments of animal bone. The top of pit F151 (~75 cm long, 60 cm wide, and ~50 cm deep) also lies below the upper boundary of LUB3 and is capped by a small pile of pebbly sandy loam sediments that contrast in color and texture with the surrounding LUB3 and LUB4 deposits (fig. S9), reminiscent of the cairn found on Area A's Pit Feature A2 (*11*). Feature 151 contained eight pieces of debitage and 16 animal bone fragments in carbonaceous pit fill.

An animal bone fragment recovered in situ within pit F78 returned two radiocarbon ages of 13,175 ± 48 yr B.P. (15,882 to 15,719 cal yr B.P.) and 13,188 ± 48 yr B.P. (15,914 to 15,740 cal yr B.P.) (Table 1). Two in situ animal bone fragments from pit F108 returned radiocarbon ages of 13,147 ± 55 yr B.P. (15,970 to 15,600 cal yr B.P.) and 13,146 ± 55 yr B.P. (15,975 to 15,590 cal yr B.P.). Three animal bone fragments recovered in situ within pit F151 returned radiocarbon ages of 13,091 ± 48 yr B.P. (15,772 to 15,617 cal yr B.P.), 13,226 ± 52 yr B.P. (15,970 to 15,790 cal yr B.P.), and 13,260 ± 240 B.P. (16,675 to 15,598 cal yr B.P.). These radiocarbon ages show that pits F78, F108, and F151 were probably created at about the same time.

Excavation of LUB3 sediments outside of these pit features found in situ 10 pieces of debitage, six animal bone fragments, and two stemmed projectile points. One of these is a fragmentary stemmed point (73-49277; Fig. 4) found in situ at an elevation of 410.846 m above sea level (masl), lying ~15 cm below the surface of F78 and therefore dates somewhat earlier. The other stemmed point (73-54105; Fig. 4) was excavated in situ above the top of pit F108 but buried within the upper limits of LUB3 sediments and thus dates sometime after the formation of the pit features but before the erosion of LUB3.

Pit features originating above LUB3

Four pit features (from oldest to youngest: F96, F99, F59, and F111) were dug downward from other LUs that lie above LUB3 in the vicinity of the composite stratigraphic profile shown in Fig. 3. None of these pits intersected F78, F108, or F151. These younger pit features contained stemmed points in forms different from those seen in LUB3, F78, and F108, an array of stone tools, FCR, debitage, and fragmentary animal bone pieces. Notably, pit F59 contained the partial skeletal remains of a wolverine (*Gulo gulo*), and the pit was capped by a hearth (*12*). Organic samples from these four younger pit features returned five accelerated mass specrometry (AMS) ages ranging between 9944 ± 39 yr B.P. (11,610 to 11,240 cal yr B.P.) and 9505 ± 38 yr B.P. (11,075 to 10,595 cal yr B.P.) (Table 1). The artifacts found in these upper deposits and younger pit features lack the heavy carbonate coatings seen on objects in LUB3 and its inclusive pit features.

Geochronology

The radiocarbon chronology of Area A was previously modeled (*1*). Here, we report a remodeling of the Area A chronology that includes 94 previously unreported radiocarbon measurements on freshwater mussel shells from LU6 (table S4). No freshwater reservoir offset was applied as seven living mussels from the Salmon River returned modern $F^{14}C$ values (table S5). Resolution for this model was set at 50 (years) to ease/speed computing (see OxCal code in the Supplementary Materials). Bayesian modeling places the start and end of LU3 at 16,500 to 15,250 and 13,450 to 11,800 cal yr B.P. (Fig. 5), in agreement with estimates previously obtained for the same stratum (*1*). LU3 is estimated to have a duration of between 2070 and 4195 years (or 2300 to 3500 years at 68.3% CI).

For Area B, Bayesian modeling of radiocarbon data identifies no major outliers and places the start of LUB3 at 16,045 to 15,725 cal yr B.P. (Fig. 6). This age range is statistically comparable to the estimate for the commencement of LU3 (equivalent) in Area A reported here but is much more tightly constrained (figs. S19 and S20). All features within LUB3 (F151, F78, and F108) are estimated to date to 15,955 to 15,625 cal yr B.P., indicating their likely contemporaneity. LUB3 is estimated to have ended at 15,845 to 15,530 cal yr B.P., considerably earlier than the estimated end of LU3 in Area A, and is attributed to the differential erosion of the LU3/LUB3 surface in Areas A and B. LUB5 likely begins at 12,965 to 11,240 cal yr B.P. following an interval of 4645 to 2755 years that is covered by optically stimulated luminescence (OSL) age 73-15-OSL-Lu2-5 at LUB4 (see the Supplementary Materials for sensitivity testing including OSL ages). Overall, the chronostratigraphic sequence shows good integrity.

The 11 late Pleistocene ^{14}C age estimates from LU3 (*1*) in Area A are largely derived from the upper half of the Hammer Creek Loess deposits (Fig. 2) (*2*–*4*), while the seven ages ranging from 13,260 ± 240 to 13,091 ± 48 ^{14}C B.P. (16,675 to 15,240 cal yr B.P.) in Area B are derived from the base of the loess unit (Fig. 2) and confirm the modeled start date for the age of the initial cultural occupation previously reported (*1*).

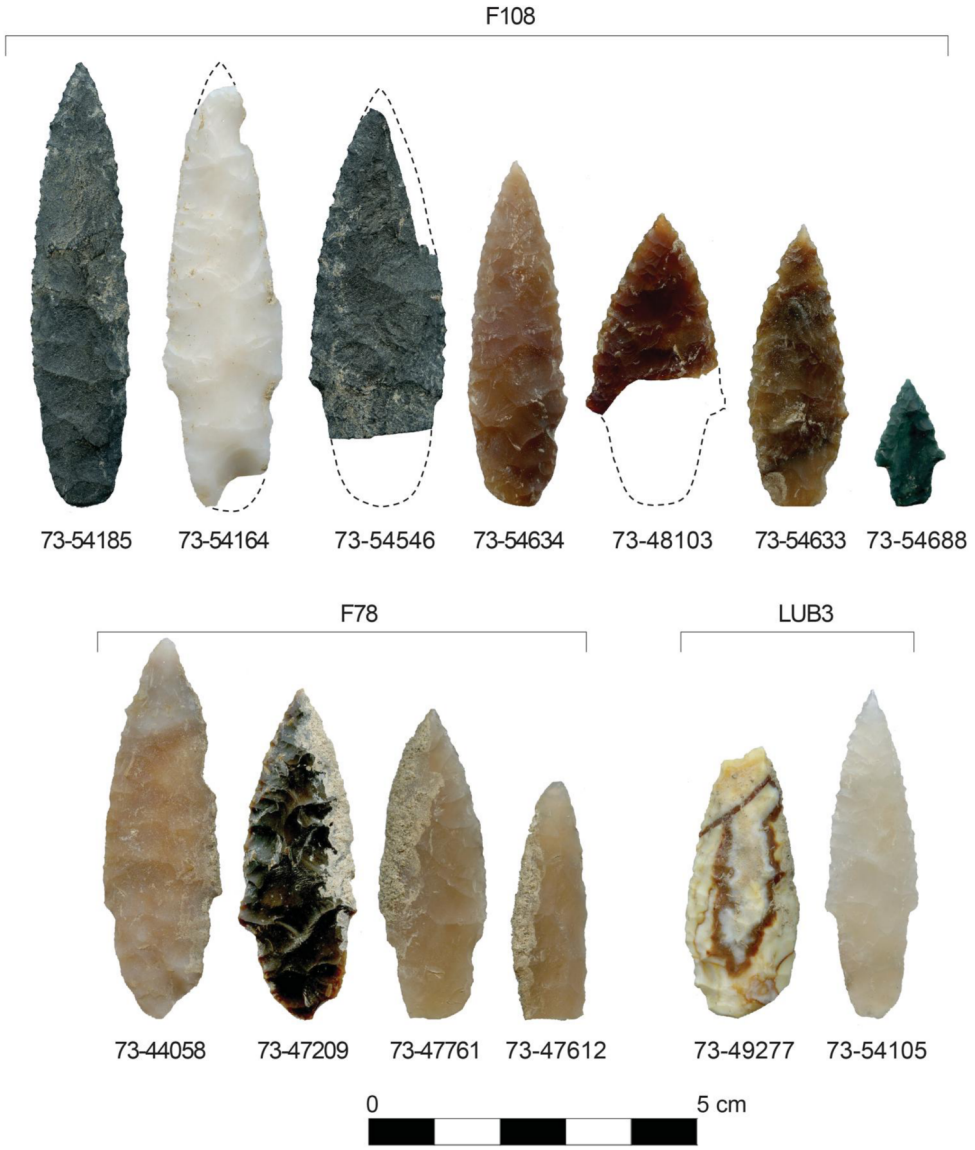

Fig. 4. Projectile points from LUB3 sediments, pit F78, and pit F108. Catalog numbers are shown beneath each point (e.g., 73-54185). Dashed lines show estimated extents. A small fragment of a probable stemmed point base found in F78 is not shown here.

Characterizing the early Cooper's Ferry lithic assemblage

Of the 14 projectile point specimens found in LUB3 and pits F78 and F108, 12 were made on cryptocrystalline silicate and 2 were made on fine-grained volcanic rock (Fig. 4). Both kinds of tool stone material are available within ~10 km of the site. Most of the projectile points are relatively small and made on elongate flakes with minimal bifacial reduction. Four larger points (73-44058, 73-54164, 73-54546, and 73-54185; Fig. 4) were more extensively reduced from bifacial preforms. The cross-sectional form of the stemmed points ranges from biconvex to plano-convex, and all show some degree of resharpening on their blade margins. The points typically show collateral flaking patterns, and several retain single beveled blade forms. The smallest stemmed point (73-54688; Fig. 4) is similar in size to a diminutive, stemmed point found at the Gault site in Texas in deposits dated by OSL to ~16 thousand years (ka) beneath a Clovis Paleoindian component (*13*). Many of the F78 and F108 points retain weak shoulders and contracting haft margins —design attributes also seen in a pre-Clovis–aged stemmed point from the Friedkin site dated to ~15.5 ka by OSL (*14*) and among points found in association with mammoth bones and a 14.5-ka tephra layer at Mexico's Santa Isabel Iztapan site (*14*–*16*). Within the Cooper's Ferry site, the haft morphometry of stemmed points changes sequentially throughout the late Pleistocene (see the supplementary materials). The early stemmed points from LUB3 and its inclusive pit features bear more subtle shoulders and contracting stem margins that make them similar to but morphometrically different from younger named stemmed point types that are known from the Pacific Northwest region (e.g., Lind Coulee and Windust), indicating a probable evolutionary relationship that requires further exploration. See the Supplementary Materials for additional discussion of projectile point morphology and the results of debitage analysis.

Table 1. AMS ages from Area B organized by laboratory number. RN is the reading number. The percent collagen is the yield of extracted collagen as a function of the starting weight of bone samples. C:N is the atomic weight ratio of carbon to nitrogen. %C is the percentage of carbon in the combusted sample. Stable isotope ratios of C and N are expressed in per mil (‰) relative to Vienna Pee Dee belemnite and ambient inhalable reservoir. The calibrations were done using the OxCal 4.3 software (*29*) and the IntCal20 calibration curve (*30*). Missing chronometric data (*) are due to a lack in reporting or measurement on behalf of the laboratories. –, not determined.

RN	Laboratory no.	Material	Northing (m)	Easting (m)	Elevation (masl)	LU	% collagen	C:N	%C	d13C (‰)	d15N (‰)	yr B.P.	± 1 SD	cal yr B.P. (95.4% CI)
44096	D-AMS 045619	Charcoal	60.394	130.680	411.889	Lower LUB16	–	–	*	*	–	1517	20	1415–1345
42302	D-AMS 045621	Charcoal	59.846	132.055	411.306	Lower LUB14, within F99	–	–	*	*	–	9658	37	11,194–11,075
26569	D-AMS 3572	Mussel shell	57.962	132.968	411.403	Lower LUB14	–	–	*	−8	–	9133	38	10,485–10,220
26568	D-AMS 3573	Mussel shell	57.679	132.758	411.379	Lower LUB14	–	–	*	−3.8	–	9106	32	10,375–10,195
26263	D-AMS 3576	Mussel shell	57.823	132.849	411.438	Lower LUB14	–	–	*	−6.2	–	9161	35	10,485–10,235
26264	D-AMS 3581	Mussel shell	57.872	132.908	411.420	Lower LUB14	–	–	*	−11.7	–	9244	36	10,555–10,255
44812	OxA-40353	Bone	58.184	132.724	410.784	Lower LUB5, within F96	6.7	3.2	44.6	−20.08	6.3	9885	31	11,395–11,220
48795	OxA-40375	Bone	59.973	131.831	410.708	LUB3, within F108	1.1	3.3	37.2	−18.87	6	13,146	59	15,975–15,585
48884	OxA-40376	Bone	57.834	133.770	411.179	Lower LUB14, within F111	0.7	3.4	41.9	−19.65	7.6	9566	34	11,095–10,730
45210	OxA-40386	Bone	58.6200	132.482	410.685	Lower LUB5, within F96	6.4	3.3	40.6	−20.11	12.5	9944	39	11,610–11,240
49224	OxA-40387	Bone	58.032	133.760	411.191	Lower LUB14, within F111	1.9	3.3	40.9	−20.14	7.6	9505	38	11,075–10,595
48817	OxA-40389	Bone	60.085	131.349	410.683	LUB3, within F108	1.7	3.3	41.5	−20.51	5	13,147	55	15,970–15,600
44450	OxA-41974	Bone	59.883	130.644	410.708	LUB3, within F151	5.7	3.2	43.6	−20.38	5.6	13,091	48	15,870–15,520
44548	OxA-41975	Bone	59.102	131.553	410.868	LUB3, within F78	2.4	3.3	42.5	−20.33	7	13,188	48	16,000–15,665
44548	OxA-41976	Bone	59.102	131.553	410.868	LUB3, within F78	2.2	3.2	42.5	−20.39	7.1	13,175	48	15,985–15,650
40205	OxA-41977	Bone	59.276	131.383	411.042	LUB4	1.8	3.3	42.4	−20.21	11.2	9572	33	11,100–10,735
44687	OxA-41978	Bone	59.872	130.753	410.634	LUB3, within F151	5.6	3.2	42.8	−20.13	5.3	13,226	52	16,055–15,700
44451	OxA-X-3172-14	Bone	59.836	130.697	410.708	LUB3, within F151	0.9	3.3	41.5	−20.27	4.3	13,260	240	16,675–15,240
44507	OxA-X-3172-15	Bone	59.041	131.283	410.739	Within displaced sediment	2.2	3.4	44.9	−20.43	14.3	9650	100	11,240–10,710
44417		Bone	59.308	131.332	410.907		0.7	3.4	42.7	−20.6	11.6	9640	120	

continued on next page

RN	Laboratory no.	Material	Northing (m)	Easting (m)	Elevation (masl)	LU	% collagen	C:N	%C	d13C (‰)	d15N (‰)	yr B.P.	± 1 SD	cal yr B.P. (95.4% CI)
	OxA-X-3172-16					Within displaced sediment								11,250–10,595
25816	UCIAMS-144543	Bone	59.507	129.740	410.177	Lower LUB14, within F59	*	*	*	−19.8	7.4	9620	35	11,175–10,775

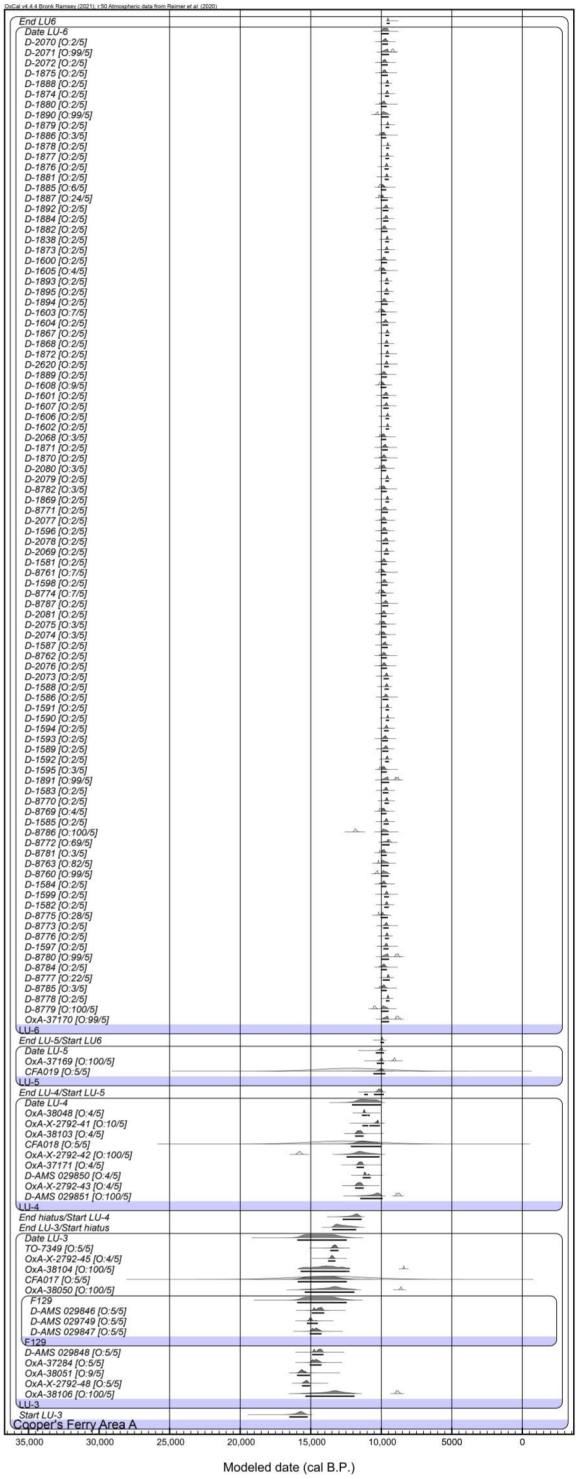

Fig. 5. Bayesian model for Cooper′s Ferry Area A. This model includes 94 previously unreported radiocarbon measurements on mussel shells from LU6 and estimates the start and end of LU3 at 16,500 to 15,250 and 13,450 to 11,800 cal yr B.P., respectively, which are comparable to previous results (*1*). Outlier analysis output is noted as "O:posterior probability/prior probability."

DISCUSSION

Combined with the previous results from the Area A excavations (*1*), there are now 18 late Pleistocene ^{14}C ages that date the cultural materials contained within the Hammer Creek Loess (LU3/LUB3) at Cooper′s Ferry. Together, these support a modeled estimate of 16,045 to 15,725 cal yr B.P. for the initial occupation at the site with intermittent occupation continuing until 13,450 to 11,800 cal yr B.P. when the loess surface was truncated by erosion. Cultural features created during this 2070-to-4195-year period (or 2300 to 3500 years at 68.3% CI) of LU3/LUB3 formation include a hearth, five storage/refuse pits, and what appears to be a food processing surface. Artifacts within the loess consist of 16 complete or fragmentary stemmed points, 30 other stone tools, 482 pieces of debitage, 355 bone fragments, including tooth enamel from an extinct horse, eight pieces of FCR, and a single fragment of freshwater river mussel shell. Fourteen of the stemmed points were deposited before the formation of the Rock Creek Soil and date to between ~16,000 and 15,600 cal yr B.P. Seven radiocarbon dates on animal bone found in direct association within two pit features bearing 12 stemmed projectile points show that humans lived at the Cooper′s Ferry site between ~16,045 and 15,725 cal yr B.P., confirming our earlier findings (*1*). The in situ discovery of a fragmentary stemmed point and other cultural materials from LUB3 loess outside of the pit features indicates that people occupied the site for some time before the dated pit features were created.

This discovery significantly expands both the radiocarbon chronology of human occupation in the Americas and our knowledge of the technological traditions used by its early inhabitants. Progenitors of the First Americans share ancestry with upper Paleolithic peoples of both southern Siberia and eastern Asia and likely became geographically isolated sometime after ~25,000 cal yr B.P. (*17*, *18*) before expanding into the Americas after ~19,500 cal yr B.P. (*19*, *20*). Paleogenetics cannot yet determine where exactly in northeast Asia these ancestors resided, so we must also rely on a close assessment of technological (stone tool) evidence to identify potential regions from which the First Americans may have originated. The nearest and most comparable projectile point form in northeast Asia that predates the ~16,000–cal yr B.P. Cooper′s Ferry occupation is associated with late upper Paleolithic (LUP) bifacial point-bearing sites in Hokkaido (figs. S12 and S13) (*9*, *21*, *22*). This LUP bifacial point tradition is preceded by a blade-point industry dating from ~32,000 to 20,000 cal yr B.P. in Hokkaido and northern Honshu (*21*). These stemmed point assemblages include both the collateral flaking and single beveled projectile point blade forms that occur in the late Pleistocene–aged stemmed points at Cooper′s Ferry (*23*). These bifacial stemmed point technologies occur well before the appearance of different lithic and ceramic technologies associated with incipient Jomon occupations in Hokkaido (~14,700 cal yr B.P.) (*24*–*25*), which may reflect the arrival of different human groups with different cultural adaptations (*25*). Dental and DNA evidence that indicate that Holocene-aged Jomon populations could not be the ancestors of the First Americans (*26*) may thus be correct but is largely irrelevant. We hypothesize that this shared similarity in pre-Jomon stemmed point technology may point to the general location along the northwest Pacific Rim from which some of the earliest peoples in the Americas may have originated between ~22,000 and 16,000 years ago (*27*, *28*).

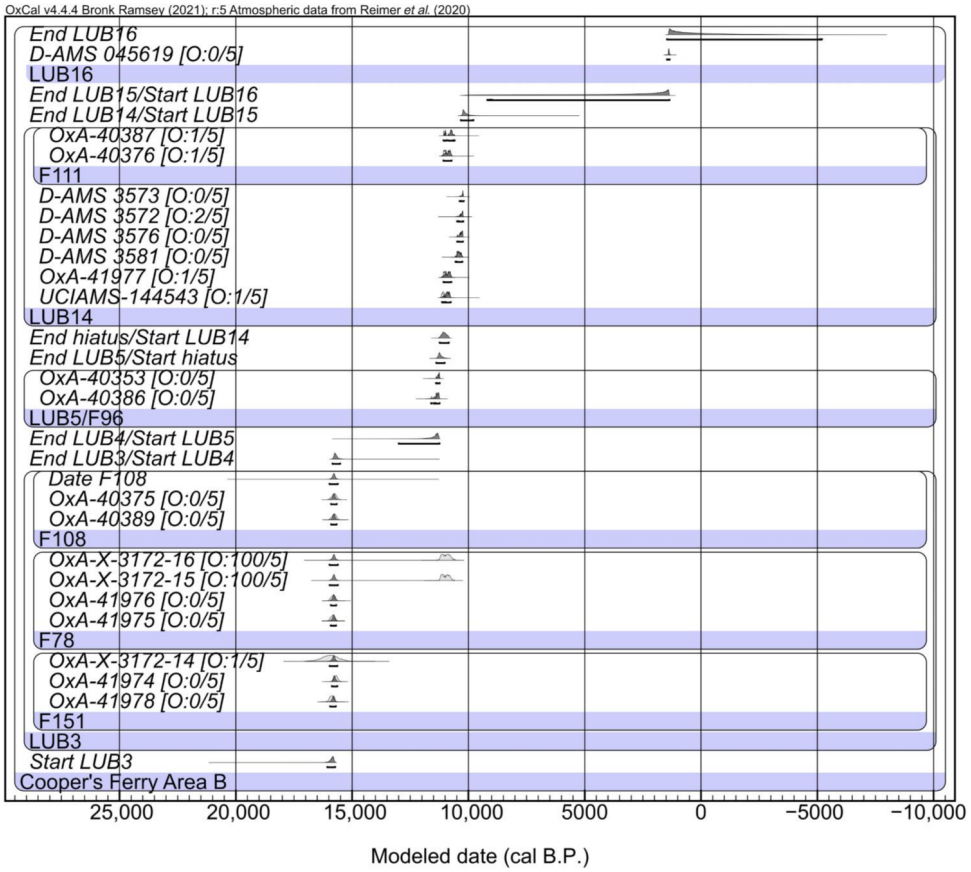

Fig. 6. Bayesian model for Cooper's Ferry Area B. This model estimates the start of LUB3 at 16,045 to 15,725 cal yr B.P. Outlier analysis output is noted as "O:posterior probability/prior probability."

MATERIALS AND METHODS

Archaeological excavations in Area B of the Cooper's Ferry site were conducted from 2012 to 2017. During this time, excavators sought to define cultural features and find items measuring ≥1 cm^2 in diameter in the ground, so that in situ total station measurements could be made of object locations. Stratigraphic information was recorded in the field during multiple field seasons. Artifact and faunal analyses, including near-infrared analysis of bone samples (see the supplementary materials), were conducted at Oregon State University. Radiocarbon samples reported from Area B were pretreated using standard methodologies at the Oxford Radiocarbon Accelerator Unit, the W.M. Keck Carbon Cycle Accelerator Mass Spectrometer Facility at the University of California, Irvine, and at the DirectAMS laboratory. Accelerator mass spectrometry dating, optically stimulated luminescence dating, and subsequent Bayesian analysis of chronometric results were performed using the protocols described in Supplementary Materials and Methods (see the supplementary materials). All radiocarbon ages were calibrated using the IntCal20 database (*30*).

Supplementary Materials

This PDF file includes:

Materials and Methods
Supplementary Text
Figs. S1 to S28
Tables S1 to S10
References

REFERENCES AND NOTES

1. L. G. Davis, D. B. Madsen, L. Becerra-Valdivia, T. Higham, D. A. Sisson, S. M. Skinner, D. Stueber, A. J. Nyers, A. Keen-Zebert, C. Neudorf, M. Cheyney, M. Izuho, F. Iizuka, S. R. Burns, C. W. Epps, S. C. Willis, I. Buvit, Late upper paleolithic occupation at Cooper's Ferry, Idaho, USA, ~16,000 years ago. *Science* **365**, 891–897 (2019).
2. JD Lancaster "Progress in the search for early sites in the lower Salmon River canyon, Idaho: A case study in geoarchaeological prospection," thesis, Oregon State University, Corvallis (2015).
3. L. G. Davis, K. Muehlenbachs, C. E. Schweger, N. W. Rutter, Differential response of vegetation to postglacial climate in the lower Salmon River canyon, Idaho. *Palaeogeogr. Palaeoclimatol. Palaeoecol.* **185**, 339–354 (2002).
4. L. G. Davis "The coevolution of early hunter-gatherer culture and riparian ecosystems in the southern Columbia River Plateau," thesis, University of Alberta, Edmonton (2001).
5. S. J. Fiedel, B. A. Potter, J. E. Morrow, M. K. Faught, C. Vance Haynes Jr., J. C. Chatters, Pioneers from Northern Japan in Idaho 16,000 Years Ago? A Critical Evaluation of the Evidence from Cooper's Ferry. *PaleoAm.* **7**, 28–42 (2020).
6. T. A. Surovell, S. A. Allaun, B. A. Crass, J. A. M. Gingerich, K. E. Graf, C. E. Holmes, R. L. Kelly, M. Kornfeld, K. E. Krasinski, M. L. Larson, S. R. Pelton, B. T. Wygal, Late date of human arrival to North America: Continental scale differences in stratigraphic integrity of pre-13,000 BP archaeological sites. *PLOS ONE* **17**, e0264092 (2022).
7. M. R. Waters, T. W. Stafford Jr., D. L. Carlson, The age of Clovis—13,050 to 12,750 cal yr B.P. *Sci. Adv.* **6**, eaaz0455 (2020).
8. L. Becerra-Valdivia, T. Higham, The timing and effect of the earliest human arrivals in North America. *Nature* **584**, 93–97 (2020).

9. Hokkaido Archaeological Operation Center, "Shirataki Isekigun VII: The Shirataki Group of Sites VII" (in Japanese) (Hokkaido Archaeological Operation Center, 2006).
10. B. R. Butler, The earlier cultural remains at Cooper's Ferry. *Tebiwa* **12**, 35–50 (1969).
11. L. G. Davis, A. J. Nyers, S. C. Willis, Context, provenance and technology of a western stemmed tradition artifact cache from the Cooper's Ferry Site, Idaho. *Am. Antiq.* **79**, 596–615 (2014).
12. A. J. Carroll "Perspectives on pits of the western stemmed tradition: An analysis on the contents of Feature 59 at the Cooper's Ferry site," thesis, Oregon State University, Corvallis (2018).
13. T. J. Williams, M. B. Collins, K. Rodrigues, W. J. Rink, N. Velchoff, A. Keen-Zebert, A. Gilmer, C. D. Frederick, S. J. Ayala, E. R. Prewitt, Evidence of an early projectile point technology in North America at the Gault Site, Texas, USA. *Sci. Adv.* **4**, eaar5954 (2018).
14. M. R. Waters, J. L. Keene, S. L. Forman, E. R. Prewitt, D. L. Carlson, J. E. Wiederhold, Pre-Clovis projectile points at the Debra L. Friedkin site, Texas—Implications for the Late Pleistocene peopling of the Americas. *Sci. Adv.* **4**, eaat4505 (2018).
15. L. A. A. de Anda, M. Maldonada-Koerdell, Association of artifacts with mammoth in the Valley of Mexico. *Am. Antiq.* **4**, 332–340 (1953).
16. L. A. A. de Anda, The second mammoth and associated artifacts at Santa Isabel Iztapan, Mexico. *Am. Antiq.* **22**, 12–28 (1956).
17. J. V. Moreno-Mayar, L. Vinner, P. de Barros Damgaard, C. de la Fuente, J. Chan, J. P. Spence, M. E. Allentoft, T. Vimala, F. Racimo, T. Pinotti, S. Rasmussen, A. Margaryan, M. I. Orbegozo, D. Mylopotamitaki, M. Wooller, C. Bataille, L. Becerra-Valdivia, D. Chivall, D. Comeskey, T. Devièse, D. K. Grayson, L. George, H. Harry, V. Alexandersen, C. Primeau, J. Erlandson, C. Rodrigues-Carvalho, S. Reis, M. Q. R. Bastos, J. Cybulski, C. Vullo, F. Morello, M. Vilar, S. Wells, K. Gregersen, K. L. Hansen, N. Lynnerup, M. M. Lahr, K. Kjær, A. Strauss, M. Alfonso-Durruty, A. Salas, H. Schroeder, T. Higham, R. S. Malhi, J. T. Rasic, L. Souza, F. R. Santos, A.-S. Malaspinas, M. Sikora, R. Nielsen, Y. S. Song, D. J. Meltzer, E. Willerslev, Early human dispersals within the Americas. *Science* **362**, eaav2621 (2018).
18. M. Raghavan, M. Steinrücken, K. Harris, S. Schiffels, S. Rasmussen, M. De Giorgio, A. Albrechtsen, C. Valdiosera, M. C. Ávila-Arcos, A.-S. Malaspinas, A. Eriksson, I. Moltke, M. Metspalu, J. R. Homburger, J. Wall, O. E. Cornejo, J. V. Moreno-Mayar, T. S. Korneliussen, T. Pierre, M. Rasmussen, P. F. Campos, P. de Barros Damgaard, M. E. Allentoft, J. Lindo, E. Metspalu, R. Rodríguez-Varela, J. Mansilla, C. Henrickson, A. Seguin-Orlando, H. Malmström, T. Stafford Jr, S. S. Shringarpure, A. Moreno-Estrada, M. Karmin, K. Tambets, A. Bergström, Y. Xue, V. Warmuth, A. D. Friend, J. Singarayer, P. Valdes, F. Balloux, I. Leboreiro, J. L. Vera, H. Rangel-Villalobos, D. Pettener, D. Luiselli, L. G. Davis, E. Heyer, C. P. E. Zollikofer, M. S. Ponce de León, C. I. Smith, V. Grimes, K.-A. Pike, M. Deal, B. T. Fuller, B. Arriaza, V. Standen, M. F. Luz, F. Ricaut, N. Guidon, L. Osipova, M. I. Voevoda, O. L. Posukh, O. Balanovsky, M. Lavryashina, Y. Bogunov, E. Khusnutdinova, M. Gubina, E. Balanovska, S. Fedorova, S. Litvinov, B. Malyarchuk, M. Derenko, M. J. Mosher, D. Archer, J. Cybulski, B. Petzelt, J. Mitchell, R. Worl, P. J. Norman, P. Parham, B. M. Kemp, T. Kivisild, C. Tyler-Smith, M. S. Sandhu, M. Crawford, R. Villems, D. G. Smith, M. R. Waters, T. Goebel, J. R. Johnson, R. S. Malhi, M. Jakobsson, D. J. Meltzer, A. Manica, R. Durbin, C. D. Bustamante, Y. S. Song, R. Nielsen, E. Willerslev, Genomic evidence for the Pleistocene and recent population history of Native Americans. *Science* **349**, aab3884 (2015).
19. B. Llamas, L. Fehren-Schmitz, G. Valverde, J. Soubrier, S. Mallick, N. Rohland, S. Nordenfelt, C. Valdiosera, S. M. Richards, A. Rohrlach, M. I. B. Romero, I. F. Espinoza, E. T. Cagigao, L. W. Jiménez, K. Makowski, I. S. L. Reyna, J. M. Lory, J. A. B. Torrez, M. A. Rivera, R. L. Burger, M. C. Ceruti, J. Reinhard, R. S. Wells, G. Politis, C. M. Santoro, V. G. Standen, C. Smith, D. Reich, S. Y. W. Ho, A. Cooper, W. Haak, Ancient mitochondrial DNA provides high-resolution time scale of the peopling of the Americas. *Sci. Adv.* **2**, e1501385 (2016).
20. T. Pinotti, A. Bergström, M. Geppert, M. Bawn, D. Ohasi, W. Shi, D. R. Lacerda, A. Solli, J. Norstedt, K. Reed, K. Dawtry, F. González-Andrade, C. Paz-Y-Miño, S. Revollo, C. Cuellar, M. S. Jota, J. E. Santos Jr., Q. Ayub, T. Kivisild, J. R. Sandoval, R. Fujita, Y. Xue, L. Roewer, F. R. Santos, C. Tyler-Smith, Y chromosome sequences reveal a short Beringian Standstill, rapid expansion, and early population structure of native american founders. *Curr. Biol.* **29**, 149–157.e3 (2019).
21. K. Morisaki, M. Izuho, K. Terry, H. Sato, Lithics and climate: Technological responses to landscape change in Upper Palaeolithic northern Japan. *Antiquity* **89**, 554–572 (2015).
22. K. Morisaki, N. Oda, D. Kunikita, Y. Sasaki, Y. Kuronuma, A. Iwase, T. Yamazaki, N. Ichida, H. Sato, Sedentism, pottery and inland fishing in late Glacial Japan: A reassessment of the Maedakochi site. *Antiquity* **93**, 1442–1459 (2019).
23. I. Y. Ponkratova, L. G. Davis, D. W. Bean, D. B. Madsen, A. J. Nyers, I. Buvit, Technological similarities between ~13 ka stemmed points from Ushki V, Kamchatka, Russia, and the earliest stemmed points in North America, in *Maritime Prehistory of Northeast Asia*, J. Cassidy, I. Ponkratova, B. Fitzhugh, Eds. (Springer Nature, 2022), pp. 233–262.
24. F. Iizuka, The timing and behavioral context of the Late-Pleistocene adoption of ceramics in greater East and Northeast Asia and the First People (without pottery) in the Americas. *PaleoAm.* **4**, 267–324 (2018).
25. D. Natsuki, Migration and adaptation of Jomon people during Pleistocene/Holocene transition period in Hokkaido, Japan. *Quat. Int.* **608-609**, 49–64 (2022).
26. G. R. Scott, D. H. O'Rourke, J. A. Raff, J. C. Tackney, L. J. Hlusko, S. A. Elias, L. Bourgeon, O. Potapova, E. Pavlova, V. Pitulko, J. F. Hoffecker, Peopling the Americas: Not "out of Japan". *PaleoAm.* **7**, 309–332 (2021).
27. L. G. Davis, D. B. Madsen, The coastal migration theory: Formulation and testable hypotheses. *Quat. Sci. Rev.* **249**, 106605 (2020).
28. I. Buvit, K. Terry, and M. Izuho, Pathways along the Pacific: Using early stone tools to reconstruct coastal migration between Japan and the Americas, in *Paleolandscapes and Archaeology*, M. T. Carson Ed. (Routledge, 2021), pp. 39–81.
29. C. B. Ramsey, Development of the radiocarbon calibration program. *Radiocarbon* **43**, 355–363 (2001).
30. P. J. Reimer, W. E. N. Austin, E. Bard, A. Bayliss, P. G. Blackwell, C. Bronk Ramsey, M. Butzin, H. Cheng, R. L. Edwards, M. Friedrich, P. M. Grootes, T. P. Guilderson, I. Hajdas, T. J. Heaton, A. G. Hogg, K. A. Hughen, B. Kromer, S. W. Manning, R. Muscheler, J. G. Palmer, C. Pearson, J. van der Plicht, R. W. Reimer, D. A. Richards, E. M. Scott, J. R. Southon, C. S. M. Turney, L. Wacker, F. Adolphi, U. Büntgen, M. Capano, S. M. Fahrni, A. Fogtmann-Schulz, R. Friedrich, P. Köhler, S. Kudsk, F. Miyake, J. Olsen, F. Reinig, M. Sakamoto, A. Sookdeo, S. Talamo, The IntCal20 Northern Hemisphere radiocarbon age calibration curve (0-55 cal kBP). *Radiocarbon* **62**, 725–757 (2020).
31. A. S. Dyke, An outline of North American deglaciation with emphasis on central and northern Canada, in *Quaternary Glaciations—Extent and Chronology. Part II: North America*, J. Ehlers, P. L. Gibbard, Eds. (Elsevier, 2004), pp. 373–424.
32. B. J. Quirk, E. Huss, B. J. C. Laabs, E. Leonard, J. Licciardi, M. A. Plummer, Late Pleistocene glacial chronologies and paleoclimate in the northern Rocky Mountains. *Clim. Past* **18**, 293–312 (2022).
33. R. B. Waitt Jr., Case for periodic, colossal jökulhlaups from Pleistocene glacial Lake Missoula. *Geol. Soc. Am. Bull.* **96**, 1271–1286 (1985).
34. R. B. Morrison, Quaternary stratigraphic, hydrologic, and climatic history of the Great Basin, with emphasis on Lakes Lahontan, Bonneville, and Tecopa, in *Quaternary Nonglacial Geology: Conterminous U.S., The Geology of North America*, vol. K-2, R. B. Morrison, Ed. (Geological Society of America, 1991), pp. 283–320.
35. J. Clark, J. X. Mitrovica, K. Latychev, Glacial isostatic adjustment in central Cascadia: Insights from three-dimensional Earth modeling. *Geology* **47**, 295–298 (2019).
36. Google Earth v.7.3.4.8642 (July 30, 2016) lower Salmon River canyon, western Idaho, USA. 445.905576° N, −116.596311° W, eye alt 627 m. Landsat 2019; www.earth.google.com [accessed 16 June 2022].
37. M. L. Schwede, "An ecological study of Nez Perce settlement patterns," thesis, Washington State University, Pullman, WA (1966).
38. L. G. Davis, D. A. Sisson, An early stemmed point cache from the lower Salmon River canyon of West-Central Idaho. *Curr. Res. Pleistocene* **15**, 12–14 (1998).
39. L. G. Davis, C. E. Schweger, Geoarchaeological context of late pleistocene and early holocene occupation at the Cooper's Ferry Site, Western Idaho, USA. *Geoarchaeology* **19**, 685–704 (2004).
40. L. G. Davis, A. J. Nyers, S. C. Willis, Context, provenance and technology of a Western Stemmed Tradition artifact cache from the Cooper's Ferry Site, Idaho. *Am. Antiq.* **79**, 596–615 (2014).
41. L. G. Davis, D. W. Bean, A. J. Nyers, Orphometric and technological attributes of western stemmed tradition projectile points revealed in a second artifact cache from the Cooper's Ferry Site, Idaho. *Am. Antiq.* **82**, 536–557 (2017).
42. P. W. Birkeland, *Soils and Geomorphology* (Oxford Univ. Press, 1984).
43. Soil Survey Division Staff, *Soil Survey Manual* (USDA handbook no. 18, U.S. Printing Office, 1993).
44. North American Commission on Stratigraphic Nomenclature (NACOSN), North American stratigraphic code. *AAPG. Bull.* **67**, 841–875 (1983).
45. K. Pye, The nature, origin and accumulation of loess. *Quat. Sci. Rev.* **14**, 653–667 (1995).
46. K. Zamanian, K. Pustovoytov, Y. Kuzyakov, Pedogenic carbonates: Forms and formation processes. *Earth Sci. Rev.* **157**, 1–17 (2016).
47. L. L. Foley, "Quaternary chronology of the Palouse loess near Washtucna, Eastern Washington," thesis, Western Washington University, Bellingham, WA (1982).
48. E. V. McDonald, A. J. Busacca, Late Quaternary stratigraphy of loess in the channeled scabland and Palouse regions of Washington State. *Quatern. Res.* **38**, 141–156 (1992).
49. M. Sponheimer, C. M. Ryder, H. Fewlass, E. K. Smith, W. J. Pestle, S. Talamo, Saving old bones: A non-destructive method for bone collagen prescreening. *Sci. Rep.* **9**, 13928 (2019).
50. J. Workman Jr., L. Weyer, *Practical Guide to Interpretative Near-Infrared Spectroscopy* (CRC Press, 2012).
51. F. Faris, M. Thorniley, Y. Wickramasinghe, R. Houston, P. Rolfe, N. Livera, A. Spencer, Non-invasive in vivo near-infrared optical measurement of the penetration depth in the neonatal head. *Clin. Phys. Physiol. Meas.* **12**, 353–358 (1991).

52. I. O. A. C. Florea, I. A. Olumegbon, C. T. Eneh, M. K. H. Malo, R. K. Korhonen, J. Töyräs, Characterizing human subchondral bone properties using near-infrared (NIR) spectroscopy. *Sci. Rep.* **8**, 9733 (2018).
53. G. H. Turner-Walker, "The characterization of fossil bone," thesis, Durham University (1993).
54. G. H. Turner-Walker, M. Jans, Reconstructing taphonomic histories using histological analysis. *Palaeogeogr. Palaeoclimatol. Palaeoecol.* **266**, 227–235 (2008).
55. C. A. Suarez, M. J. Kohn, Caught in the act: A case study on microscopic scale physicochemical effects of fossilization on stable isotopic composition of bone. *Geochim. Cosmochim. Acta* **268**, 277–295 (2020).
56. C. B. Ramsey, Bayesian analysis of radiocarbon dates. *Radiocarbon* **51**, 337–360 (2009).
57. C. B. Ramsey, Dealing with outliers and offsets in radiocarbon dating. *Radiocarbon* **51**, 1023–1045 (2009).
58. A. S. Murray, A. G. Wintle, The single aliquot regenerative dose protocol: Potential for improvements in reliability. *Radiat. Meas.* **37**, 377–381 (2003).
59. G. Duller, Distinguishing quartz and feldspar in single grain luminescence measurements. *Radiat. Meas.* **37**, 161–165 (2003).
60. P. Liang, S. L. Forman, LDAC: An Excel-based program for luminescence equivalent dose and burial age calculations. *Ancient TL* **37**, 21–40 (2019).
61. G. Li, F. Chen, D. Xia, H. Yang, X. Zhang, D. Madsen, C. Oldknow, H. Wei, Z. Rao, M. Qiang, A Tianshan Mountains loess-paleosol sequence indicates anti-phase climatic variations in arid Center Asia and in East Asia. *Earth Planet. Sci. Lett.* **494**, 153–163 (2018).
62. L. G. Davis, Paleoseismicity and prehistoric anadromous fish exploitation in the salmon river basin, Western Idaho. *N. Amer. Arch.* **23**, 233–263 (2008).
63. E. J. Rhodes, Optically stimulated luminescence dating of sediments over the past 200,000 years. *Annu. Rev. Earth Planet. Sci.* **39**, 461–488 (2011).
64. L. G. Davis, D. W. Bean, A. J. Nyers, D. R. Brauner, GLiMR: A GIS-based method for the geometric morphometric analysis of Artifacts. *Lithic Technol.* **40**, 199–217 (2015).
65. A. Steffen, E. J. Skinner, P. W. Ainsworth, A view to the core: Technological units and debitage analysis, in *Unit Issues in Archaeology: Measuring Time, Space, and Material*, A. F. Ramenofsky, A. Steffen, Eds. (University of Utah Press, 1997), pp. 131–146.
66. T. L. Ozbun, D. O. Stueber, M. Zehendner, J. L. Fagan, Lithic debitage and formed tools, in *Marmes Rockshelter: A Final Report on 11,000 Years of Cultural Use*, B. A. Hicks, Ed. (Washington State University Dent. Press, 2004), pp. 159–227.
67. F. Sellet, Chaine operatoire: The concept and its applications. *Lithic Technol.* **18**, 106–112 (1993).
68. N. Toth, K. Schick, in *The Cutting Edge: New Approaches to the Archaeology of Human Origins*, K. Schick, N. Toth, Eds. (Stone Age Institute, 2009), pp. 267–344.
69. L. G. Davis, S. C. Willis, in *Convergent Evolution and Stone-Tool Technology*, M. O'Brien, M. Eren, B. Buchannan, Eds. (MIT Press, 2018), pp. 253–274.
70. R. E. Clopton, Standard nomenclature and metrics of plane shapes for use in Gregarine Taxonomy. *Comp. Parasitol.* **73**, 130–140 (2004).
71. P. D. Polly, L. Killick, M. Ruddy, Using left-right asymmetry to estimate non-genetic variation in vole teeth (*Arvicolinae*, *Muridae*, *Rodentia*). *Palaeontol. Electron.* **14**, 1–12 (2011).

Acknowledgments: L.G.D. thanks the Nez Perce Tribe and N. Williamson Cloud for the support on archaeological research at the Cooper's Ferry site. The Area B excavations were performed by archaeology field school staff members, students, and interns from Oregon State University (2012 to 2017) and the Nez Perce tribe (2016 to 2017). **Funding:** Cooper's Ferry project work in Area B was funded through challenge cost share agreements between the Bureau of Land Management's Cottonwood Field Office and Oregon State University (2012 to 2019; assistance agreements L09AC15147 and L14AC00232), by the Bernice Peltier Huber Charitable Trust, the Keystone Archaeological Research Fund, the National Geographic Society (2013, "Exploring Western Stemmed Tradition Archaeology at the Cooper's Ferry Site, Idaho"), and Oregon State University. **Author contributions:** L.G.D., D.A.S., and F.K.H. directed Area B excavations and archaeological project management. L.G.D. and D.B.M. conducted geoarchaeological investigations and wrote the corresponding Supplementary Materials section. L.G.D., D.S., D.W.B., and A.C. conducted the artifact and feature analysis and wrote the corresponding Supplementary Materials section. C.W.E. and L.G.D. conducted archaeofaunal bone analyses and wrote the corresponding Supplementary Materials section. C.R. and M.S. conducted near infrared analysis of bone samples in advance of radiocarbon dating and wrote the corresponding Supplementary Materials section. L.V.-B. and T.H. conducted the Bayesian modeling and wrote corresponding main text and Supplementary Materials sections. G.L. and D.B.M. conducted the OSL analysis and wrote the corresponding Supplementary Materials section. L.G.D., D.B.M., D.A.S., M.I., and F.I. wrote the introduction,results, and discussion. All authors reviewed the final draft. **Competing interests:** The authors declare that they have no competing interests. **Data and materials availability:** All data needed to evaluate the conclusions in the paper are present in the paper and/or the Supplementary Materials. The Cooper's Ferry archaeological collection is curated at the Department of Anthropology of Oregon State University.

Submitted 27 July 2022
Accepted 10 November 2022
Published 23 December 2022
10.1126/sciadv.ade1248

ScienceDaily®
Your source for the latest research news

Bering Land Bridge formed surprisingly late during last ice age

Date: December 26, 2022

Source: University of California - Santa Cruz

Summary: A new study that reconstructs the history of sea level at the Bering Strait shows that the Bering Land Bridge connecting Asia to North America did not emerge until around 35,700 years ago, less than 10,000 years before the height of the last ice age (known as the Last Glacial Maximum). The findings indicate that the growth of the ice sheets -- and the resulting drop in sea level -- occurred surprisingly quickly and much later in the glacial cycle than previous studies had suggested.

FULL STORY

A new study that reconstructs the history of sea level at the Bering Strait shows that the Bering Land Bridge connecting Asia to North America did not emerge until around 35,700 years ago, less than 10,000 years before the height of the last ice age (known as the Last Glacial Maximum).

The new findings, published the week of December 26 in *Proceedings of the National Academy of Sciences*, indicate that the growth of the ice sheets -- and the resulting drop in sea level -- occurred surprisingly quickly and much later in the glacial cycle than previous studies had suggested.

"It means that more than 50 percent of the global ice volume at the Last Glacial Maximum grew after 46,000 years ago," said Tamara Pico, assistant professor of Earth and planetary sciences at UC Santa Cruz and a corresponding author of the paper. "This is important for understanding the feedbacks between climate and ice sheets, because it implies that there was a substantial delay in the development of ice sheets after global temperatures dropped."

Global sea levels drop during ice ages as more and more of Earth's water gets locked up in massive ice sheets, but the timing of these processes has been hard to pin down.

During the Last Glacial Maximum, which lasted from about 26,500 to 19,000 years ago, ice sheets covered large areas of North America. Dramatically lower sea levels uncovered a vast land area known as Beringia that extended from Siberia to Alaska and supported herds of horses, mammoths, and other Pleistocene fauna. As the ice sheets melted, the Bering Strait became flooded again around 13,000 to 11,000 years ago.

The new findings are interesting in relation to human migration because they shorten the time between the opening of the land bridge and the arrival of humans in the Americas. The timing of human migration into North America remains unresolved, but some studies suggest people may have lived in Beringia throughout the height of the ice age.

"People may have started going across as soon as the land bridge formed," Pico said.

The new study used an analysis of nitrogen isotopes in seafloor sediments to determine when the Bering Strait was flooded during the past 46,000 years, allowing Pacific Ocean water to flow into the Arctic Ocean. First author Jesse Farmer at Princeton University led the isotope analysis, measuring nitrogen isotope ratios in the remains of marine plankton preserved in sediment cores collected from the seafloor at three locations in the western Arctic Ocean. Because of differences in the nitrogen composition of Pacific and Arctic waters, Farmer was able to identify a nitrogen isotope signature indicating when Pacific water flowed into the Arctic.

Pico, whose expertise is in sea level modeling, then compared Farmer's results with sea level models based on different scenarios for the growth of the ice sheets.

"The exciting thing to me is that this provides a completely independent constraint on global sea level during this time period," Pico said. "Some of the ice sheet histories that have been proposed differ by quite a lot, and we were able to look at what the predicted sea level would be at the Bering Strait and see which ones are consistent with the nitrogen data."

The results support recent studies indicating that global sea levels were much higher prior to the Last Glacial Maximum than previous estimates had suggested, she said. Average global sea level during the Last Glacial Maximum was about 130 meters (425 feet) lower than today. The actual sea level at a particular site such as the Bering Strait, however, depends on factors such as the deformation of the Earth's crust by the weight of the ice sheets.

"It's like punching down on bread dough -- the crust sinks under the ice and rises up around the edges," Pico said. "Also, the ice sheets are so massive they have gravitational effects on the water. I model those processes to see how sea level would vary around the world and, in this case, to look at the Bering Strait."

The findings imply a complicated relationship between climate and global ice volume and suggest new avenues for investigating the mechanisms underlying glacial cycles.

In addition to Pico and Farmer, the coauthors include Ona Underwood and Daniel

Sigman at Princeton University; Rebecca Cleveland-Stout at the University of Washington; Julie Granger at the University of Connecticut; Thomas Cronin at the U.S. Geological Survey; and François Fripiat, Alfredo Martinez-Garcia, and Gerald Haug at the Max Planck Institute for Chemistry in Germany. This work was supported by the National Science Foundation.

Story Source:

Materials provided by **University of California - Santa Cruz**. Original written by Tim Stephens. *Note: Content may be edited for style and length.*

Journal Reference:

1. Jesse R. Farmer, Tamara Pico, Ona M. Underwood, Rebecca Cleveland Stout, Julie Granger, Thomas M. Cronin, François Fripiat, Alfredo Martínez-García, Gerald H. Haug, Daniel M. Sigman. **The Bering Strait was flooded 10,000 years before the Last Glacial Maximum**. *Proceedings of the National Academy of Sciences*, 2022; 120 (1) DOI: 10.1073/pnas.2206742119

Cite This Page:

PNAS RESEARCH ARTICLE | EARTH, ATMOSPHERIC, AND PLANETARY SCIENCES OPEN ACCESS

The Bering Strait was flooded 10,000 years before the Last Glacial Maximum

Jesse R. Farmer[a,b,1], Tamara Pico[c,1], Ona M. Underwood[a], Rebecca Cleveland Stout[d,2], Julie Granger[e], Thomas M. Cronin[f], François Fripiat[b,g], Alfredo Martínez-García[b], Gerald H. Haug[b,h], and Daniel M. Sigman[a]

Edited by Claire Waelbroeck, Laboratoire d'Océanographie et du Climat: Expérimentations et Approches Numériques, Institut Pierre-Simon Laplace, Paris, France; received April 18, 2022; accepted October 21, 2022 by Editorial Board Member Jean Jouzel

The cyclic growth and decay of continental ice sheets can be reconstructed from the history of global sea level. Sea level is relatively well constrained for the Last Glacial Maximum (LGM, 26,500 to 19,000 y ago, 26.5 to 19 ka) and the ensuing deglaciation. However, sea-level estimates for the period of ice-sheet growth before the LGM vary by > 60 m, an uncertainty comparable to the sea-level equivalent of the contemporary Antarctic Ice Sheet. Here, we constrain sea level prior to the LGM by reconstructing the flooding history of the shallow Bering Strait since 46 ka. Using a geochemical proxy of Pacific nutrient input to the Arctic Ocean, we find that the Bering Strait was flooded from the beginning of our records at 46 ka until $35.7^{+3.3}_{-2.4}$ ka. To match this flooding history, our sea-level model requires an ice history in which over 50% of the LGM's global peak ice volume grew after 46 ka. This finding implies that global ice volume and climate were not linearly coupled during the last ice age, with implications for the controls on each. Moreover, our results shorten the time window between the opening of the Bering Land Bridge and the arrival of humans in the Americas.

Arctic Ocean | Bering Strait | sea level | foraminifera-bound N isotopes | glacial isostatic adjustment

Significance

The Bering Strait was a land bridge during the peak of the last ice age (the Last Glacial Maximum, LGM), when sea level was ~130 m lower than today. This study reconstructs the history of sea level at the Bering Strait by tracing the influence of Pacific waters in the Arctic Ocean. We find that the Bering Strait was open from at least 46,000 until 35,700 y ago, thus dating the last formation of the land bridge to within 10,000 y of the LGM. This history requires that ice volume increased rapidly into the LGM. In addition, it appears that humans migrated to the Americas as soon as the formation of the land bridge allowed for their passage.

The Bering Strait, the ~53 m deep ocean passage that separates Asia from North America (1), is the only Northern Hemisphere connection between the Pacific and Atlantic Oceans. Today, ~1 Sv (10^6 m^3 s^{-1}) of low-salinity Pacific seawater flows northward across the Bering Strait (2) and contributes to the relative freshness of the upper Arctic Ocean (Fig. 1). Export of these Arctic waters into the subpolar North Atlantic modifies the surface waters that form North Atlantic Deep Water (3) and may cause feedbacks between the North Pacific and North Atlantic Oceans (4–6).

During the last glacial cycle, sea-level changes driven by the growth and decay of continental ice sheets exposed and flooded the Bering Strait. The Bering Strait flooded most recently between 13 and 11 ka during sea-level rise caused by the melting of ice sheets (11, 12). Before 13 ka, the Bering Strait was subaerially exposed due to lowered sea level from extensive continental ice sheets during the Last Glacial Maximum (LGM) (26.5 to 19 ka, ref. (13)) and early deglaciation. At this time, Asia and North America were connected by the Bering Land Bridge, a proposed route by which human populations first entered the Americas (14–16). However, there is great uncertainty as to the timing with which ice growth leading up to the LGM exposed the Bering Strait and formed the Bering Land Bridge. Hopkins (14) initially reported geological evidence for Bering Strait submergence prior to the LGM, but this evidence is debated (17).

Relative sea level at the Bering Strait (RSL_{BeSt}) is affected by global mean sea level (GMSL) and the solid Earth response to the growth and decay of ice sheets through the process of glacial isostatic adjustment (11). Uncertainty regarding Bering Strait submergence prior to the LGM reflects the correspondingly high uncertainty as to the history of GMSL leading up to the LGM. Estimates of GMSL between 50 and 30 ka from various geological and geochemical data range between −25 and −105 m (Fig. 2*B*, refs. (18–24)). This GMSL uncertainty of > 60 m, which exceeds the entire sea-level equivalent of the modern Antarctic Ice Sheet (58 m, (25)), reflects in part the paucity of geological sea-level observations: Advancing ice sheets razed evidence of prior ice margins (26), and sea-level rise during the last deglaciation destroyed or submerged ancient coastlines. In addition, radiometrically dated coral sea-level markers are limited to uplifted terraces during this time, with reconstructed paleo-elevations that are subject to errors in uplift corrections (27, 28).

The submergence history of the Bering Strait is important in diverse contexts. First, considering its modern sill depth of −53 m, the Bering Strait's submergence history, when corrected for glacial isostatic adjustment, could serve as a critically needed constraint on

Author contributions: J.R.F., T.P., and D.M.S. designed research; J.R.F., T.P., O.M.U., R.C.S., J.G., T.M.C., and F.F. performed research; J.R.F., T.P., and T.M.C. contributed new reagents/analytic tools; J.R.F., T.P., O.M.U., R.C.-S., J.G., F.F., A.M.-G., G.H.H., and D.M.S. analyzed data; and J.R.F., T.P., J.G., T.M.C., F.F., A.M.-G., G.H.H., and D.M.S. wrote the paper.

The authors declare no competing interest.

This article is a PNAS Direct Submission. C.W. is a guest editor invited by the Editorial Board.

[1]To whom correspondence may be addressed. Email: jesse.farmer@umb.edu or tpico@ucsc.edu.

[2]Present address: Department of Atmospheric Sciences, University of Washington, Seattle, WA 98195.

This article contains supporting information online at https://www.pnas.org/lookup/suppl/doi:10.1073/pnas.2206742119/-/DCSupplemental.

Published December 27, 2022.

GMSL between 50 and 30 ka. If RSL_{BeSt} is closely correlated with GMSL, sea-level inferences from the ICE-5G global ice sheet history (19) (black line, Fig. 2*B*), oxygen isotope records in the Red Sea (20) (red line, Fig. 2*B*), and a stacked sea-level equivalent oxygen isotope record (21) (blue line, Fig. 2*B*) suggest that the Bering Strait would have been subaerially exposed during this time, whereas recent GMSL estimates based on glacial isostatic adjustment analyses of sea-level data (22, 23) (purple line, Fig. 2*B*) and ice margin constraints (24) (gray line, Fig. 2*B*) indicate that the Bering Strait would have been submerged. Second, the Bering Strait's sea-level history impacts the connectivity of the Pacific and Atlantic Oceans, which has been hypothesized to control abrupt (millennial-scale) climate and ocean circulation variability during the last ice age (5, 6). Third, the submergence history affects when terrestrial migrations were possible between Asia and North America across the Bering Land Bridge, putatively leading to the first arrival of humans in North America.

Here, we reconstruct the history of Bering Strait submergence since 46 ka using a geochemical proxy for Pacific water input to the western Arctic Ocean (8) and simulations of relative sea level at the Bering Strait (11, 30). These reconstructions show that, contrary to previous assumptions (5, 6) and congruent with the original hypothesis of Hopkins (14), the Bering Strait was flooded by at least 46 ka and that the Bering Land Bridge formed only after ~36 ka.

The geochemical proxy for Bering Strait submergence is based on regional features of the marine nitrogen (N) cycle in the polar Northern hemisphere oceans. The N isotopic composition ($\delta^{15}N = [(^{15}N/^{14}N)_{sample}/(^{15}N/^{14}N)_{air} - 1] * 1000$) of nitrate ($NO_3^-$), the primary form of fixed N supplied to surface ocean ecosystems, varies by about 3 parts per thousand (3‰) among the high-latitude North Atlantic, North Pacific, and western Arctic Oceans today (Fig. 1*A*). Specifically, the $\delta^{15}N$ of nitrate supplied to the surface mixed layer is substantially higher in the western Arctic (~8‰) than in the eastern Arctic or subpolar North Atlantic (~5‰). The high western Arctic nitrate $\delta^{15}N$ arises from two features unique to the Pacific inflow across the Bering Strait. First, the nitrate inflow across the Bering Strait is elevated in $\delta^{15}N$ relative to the high-latitude North Atlantic Ocean. This reflects both the higher nitrate $\delta^{15}N$ in subarctic North Pacific subsurface waters relative to subarctic North Atlantic waters (*SI Appendix*, Fig. S1) due to water column denitrification in the North Pacific interior, and partial nitrate assimilation in Bering Sea surface waters (32). Second, the high nitrate concentration of this Bering Strait inflow fuels high shelf productivity, which in turn initiates coupled partial nitrification-denitrification (CPND) on the Bering Sea shelf and the western Arctic shelves; this CPND further elevates nitrate $\delta^{15}N$ (33–36). Importantly, the Arctic Ocean's CPND is sited exclusively in areas that are influenced by the Bering Strait inflow (33–36) (*SI Appendix*, section S2 and Figs. S1 and S2). Accordingly, the subsurface nitrate $\delta^{15}N$ elevation in the western Arctic is directly tied to Pacific nitrate input (Fig. 1*A*).

We reconstruct the N isotope signature associated with the Bering Strait inflow back to 46 ka by measuring the $\delta^{15}N$ of organic matter bound within the planktonic foraminifer *Neogloboquadrina pachyderma* (hereafter, $\delta^{15}N_{N.p.}$) from three sediment cores in the western Arctic Ocean and, as a control, from one core in the central Arctic Ocean outside the direct influence of the Bering Strait inflow (Fig. 1*A*). Planktonic foraminifera-bound $\delta^{15}N$ (such as $\delta^{15}N_{N.p.}$) reflects the $\delta^{15}N$ of organic matter produced in surface waters (8, 37), which depends on the $\delta^{15}N$ of the subsurface nitrate supply and the degree of nitrate consumption, that is, the summertime drawdown of nitrate as a proportion of annual nitrate supply (38). Summertime nitrate consumption is complete in the western Arctic today due to the highly stratified upper water column (39), which arises in part from continual supply of low-salinity seawater across the Bering Strait (8) (Fig. 1).

Farmer et al. (8) showed that western Arctic $\delta^{15}N_{N.p.}$ recorded the most recent postglacial flooding of the Bering Strait, which has been dated by independent methods to 13 to 11 ka (e.g., refs. (11) and (12)) (Fig. 2*D*). During Marine Isotope Stage (MIS) 2 (29 to 11.7 ka, including the LGM), western Arctic $\delta^{15}N_{N.p.}$ ranged from 4.5 to 6‰, requiring Atlantic-sourced nitrate as well as incomplete nitrate consumption due to weaker density stratification (8). Around 11.5 ka, western Arctic $\delta^{15}N_{N.p.}$ rapidly rose to values of 7.8 to 8.8‰ throughout the Holocene. This $\delta^{15}N_{N.p.}$ rise resulted from flooding of the Bering Strait, which introduced nitrate-rich, high-$\delta^{15}N$ Pacific waters, triggered shelf

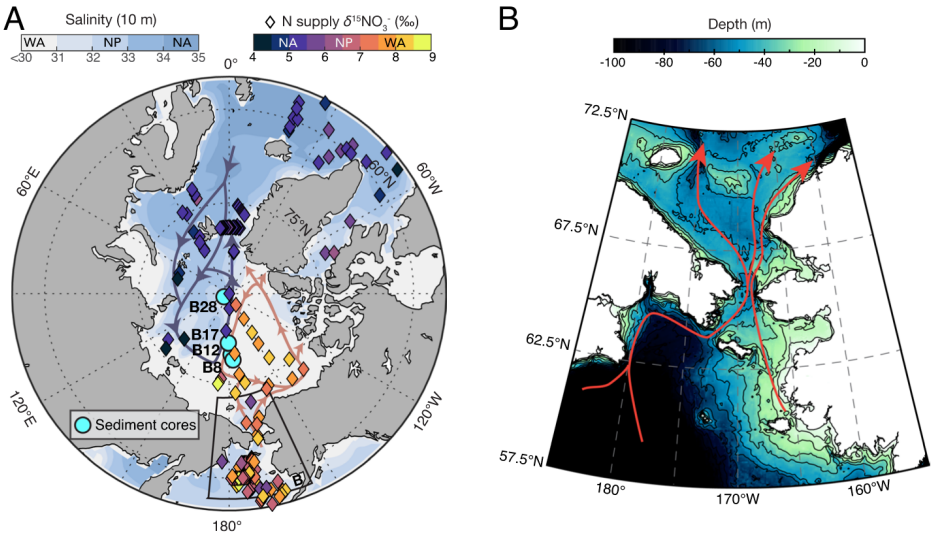

Fig. 1. Hydrography of the polar Northern Hemisphere and Bering Strait bathymetry. (*A*) Mixed layer (10 m depth) salinity (7) (blue shading) and subsurface (~50 to 200 m) nitrogen isotopic composition ($\delta^{15}N$) of nitrate (diamonds). From published data sets, sample depths were chosen to capture the nitrate being supplied to the mixed layer in the Arctic and North Atlantic (NA), and the North Pacific (NP) nitrate being transported across the Bering Strait (see data sources and selection criteria in *SI Appendix*, section S2). The mean salinity and nitrate $\delta^{15}N$ values for the western Arctic (WA), NP, and NA are indicated on the color bars. Cyan circles show locations of sediment cores; light blue and orange arrows show schematic circulation of Atlantic- and Pacific-sourced nitrate-rich subsurface waters, respectively (8, 9). (*B*) Bering Strait bathymetry (1) contoured at 10 m intervals. Red lines indicate principal ocean transport pathways (10).

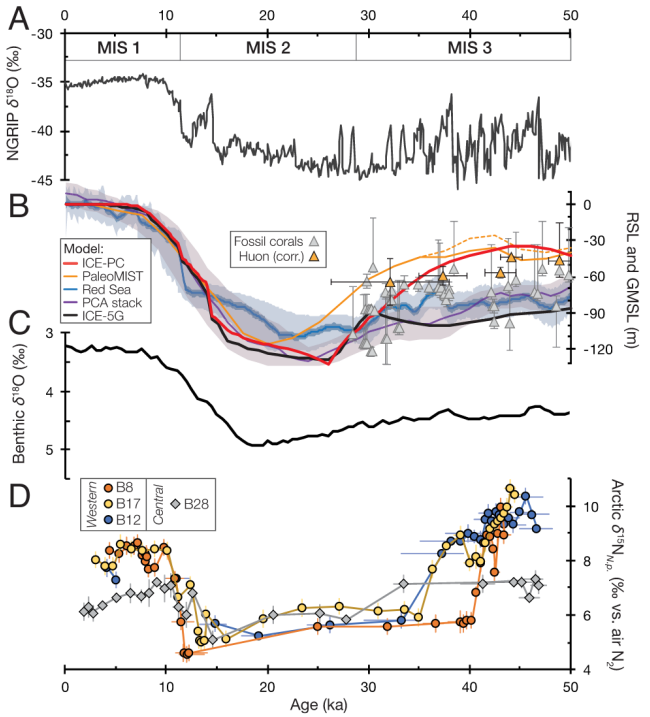

Fig. 2. Arctic Ocean foraminifera-bound N isotope records compared with related records of climate and sea-level change since 50 ka. (*A*) NGRIP ice core δ^{18}O, reflecting Greenland air temperature (29). (*B*) Sea-level reconstructions from ICE-5G (19) (black), the Red Sea (20) (blue-red shading), stacked oxygen isotope-based sea-level reconstructions (21) (purple with purple shading), PaleoMIST (24) (orange, dashed line is minimal MIS 3 GMSL scenario), ICE-PC (red, this study and ref. (30)), previously published MIS 3 coral sea-level benchmarks (27) (gray triangles), and recently corrected Huon Peninsula sea-level datums (28) (yellow triangles). (*C*) Global benthic foraminifera δ^{18}O stack (31), which records both global ice volume and deep ocean temperature and is widely applied as a sea-level proxy. (*D*) Western (circles) and central (gray diamonds) Arctic Ocean $\delta^{15}N_{N.p.}$ (this study); vertical error bars denote the larger of measured or long-term replicate $\delta^{15}N_{N.p.}$ precision (*Methods*), and horizontal error bars denote 68% quantiles (equivalent to ±1sd) of the age-depth model. Timing of MIS 1 to 3 according to (31) is denoted at the top.

CPND that further elevated nitrate δ^{15}N in the western Arctic, and stratified the upper water column, leading to complete nitrate consumption (8).

New $\delta^{15}N_{N.p.}$ records from three western Arctic Ocean sediment cores extend these reconstructions to the limit of radiocarbon dating (~50 ka), through the pre-LGM interval of larger sea-level uncertainty (Fig. 2). Results exhibit three distinct intervals separated by two rapid transitions. The youngest transition, a $\delta^{15}N_{N.p.}$ rise of ~3‰ around 11 ka, records the postglacial flooding of the Bering Strait discussed above, ending the low $\delta^{15}N_{N.p.}$ (of 4.5 to 6‰) of MIS 2. The new data show that the low $\delta^{15}N_{N.p.}$ of MIS 2 did not extend back through MIS 3 (57 to 29 ka). Instead, all the three western Arctic sites show high $\delta^{15}N_{N.p.}$ values of 8 to 10.5‰ prior to 35 to 40 ka; these values are equivalent to or higher than Holocene $\delta^{15}N_{N.p.}$ at these locations. Moreover, western Arctic $\delta^{15}N_{N.p.}$ values are 2 to 3.5‰ higher than those measured in the central Arctic before 35 to 40 ka (Fig. 2*D*). Western and central Arctic $\delta^{15}N_{N.p.}$ values converge after 35 ka, with similar $\delta^{15}N_{N.p.}$ values (of 4.5 to 6‰) lasting in both regions until 11 ka.

Moving forward in time from MIS 3, all the three western Arctic cores show a ~3‰ $\delta^{15}N_{N.p.}$ decline within 2 cm of sediment (equating to 1 to 2 kyr based on age models; *SI Appendix*, section S1 and Fig. S3). Radiocarbon age models (*SI Appendix*, Fig. S3) date this transition to 40 ka at B8 and 35 ka at B12 and B17 (*SI Appendix*, Fig. S5*A*). The data are consistent with a simultaneous $\delta^{15}N_{N.p.}$ decline in all the three cores, given the age model uncertainties of up to ±3 ka (95% CI) (*SI Appendix*, Fig. S5) and also considering the potential effects of bioturbation at these low sedimentation rates. Conversely, it would be difficult to explain different timings in the large and similar magnitude of $\delta^{15}N_{N.p.}$ decline at these three proximal western Arctic cores (which are all located within 360 km of one another; Fig. 1*A*). Moreover, true diachrony in the $\delta^{15}N_{N.p.}$ decline among sites is inconsistent with the decline in $\delta^{15}N_{N.p.}$ occurring first at Site B8, which is the site closest to the Bering Strait (Fig. 1*A*) and so would presumably be the last site to lose an isotopic signal emanating from the Strait. Thus, we consider that the $\delta^{15}N_{N.p.}$ decline is contemporaneous at these locations and assign a median (± interquartile range) age for the transition of $35.7^{+3.3}_{-2.4}$ ka (*SI Appendix*, Fig. S5*A*).

The MIS 3 western Arctic $\delta^{15}N_{N.p.}$ records require the presence of a high-δ^{15}N nitrate source that was rapidly removed around 36 ka. A terrigenous N source can be excluded, as both dissolved and particulate nitrogen inputs from Arctic rivers are too low in δ^{15}N [2 to 5‰; (40, 41)] to explain the elevated western Arctic $\delta^{15}N_{N.p.}$ values. This is also supported by low nitrate δ^{15}N (<5‰) in the Kara Sea and the Laptev Sea, where large terrigenous N contributions are expected (Fig. 1*A* and *SI Appendix*, Fig. S2). Additionally, our central Arctic $\delta^{15}N_{N.p.}$ record (gray diamonds in Fig. 2*D*) requires that the high-δ^{15}N nitrate was limited to the western Arctic during MIS 3, as occurs today (Fig. 1). The central Arctic $\delta^{15}N_{N.p.}$ record averages 7.1‰ prior to 35 ka; this value is consistent with foraminifera-bound δ^{15}N records from the North Atlantic that indicate a regional upper water column nitrate δ^{15}N of 5 to 6‰ during MIS 3 (42). Thus, the central Arctic most likely received nitrate from the North Atlantic Ocean during MIS 3, as occurred throughout the last 35 kyr (8). The $\delta^{15}N_{N.p.}$ homogeneity of the western and central Arctic between 35 and 11 ka (Fig. 2*D*) points to similar North Atlantic nitrate sources and a shared condition of weak upper ocean stratification in the two regions (8). Finally, the spatial gradient in $\delta^{15}N_{N.p.}$ between the western and central Arctic that occurred prior to ~36 ka redeveloped by 11 ka with the deglacial flooding of the Bering Strait. Thus, from an N isotopic perspective, MIS 3 and the Holocene appear remarkably similar in the Arctic (Fig. 2).

Given the above evidence, we conclude that the Bering Strait was flooded prior to ~36 ka. With a flooded Bering Strait, high-δ^{15}N nitrate from the Bering Sea would have been transported northward into the western Arctic Ocean as occurs today (33–36) (*SI Appendix*, Fig. S2). High nutrient concentrations in these Bering Strait inflow waters would also have fueled high primary productivity at the shelf break, triggering CPND that further elevates nitrate δ^{15}N in the western Arctic today (Fig. 1 and *SI Appendix*, section S3 and Fig. S1*D*). Finally, nitrate consumption in the western Arctic is complete due to the strong density stratification of the region, which appears contingent on the low-salinity Bering Strait inflow (8). The existence of this inflow before 36 ka may have strengthened western Arctic stratification at that time, leading to more complete surface ocean nitrate consumption in the western Arctic, and this may be required to reach the high $\delta^{15}N_{N.p.}$ of MIS 3.

It is noteworthy that western Arctic $\delta^{15}N_{N.p.}$ is higher between 40 and 46 ka than during the Holocene. This could reflect a greater extent of halocline and surface waters influenced by the Bering Strait inflow in the former period, enhanced CPND on the Bering Sea and western Arctic shelves, and/or a higher δ^{15}N of the subarctic North Pacific nitrate source flowing onto the Bering Sea shelf due to more complete summertime nitrate consumption in the Bering Sea, as suggested by higher diatom-bound δ^{15}N in the Bering Sea during MIS 3 (43). While our current data do not distinguish among these explanations, a flooded Bering Strait during MIS 3 is required in all cases.

After ~36 ka, the rapid $\delta^{15}N_{N.p.}$ decline at all three western Arctic sites and $\delta^{15}N_{N.p.}$ values of <7‰ indicate the cessation of the Bering Strait inflow to the Arctic, following the same logic as outlined above (*SI Appendix*, section S3). This reflects the subaerial exposure of the Bering Strait and thus formation of the Bering Land Bridge, with a terrestrial connection persisting through the LGM (11, 12, 14, 17).

To assess the quantitative implications of our findings for global ice volume during MIS 3, we model glacial isostatic adjustment and relative sea level at the Bering Strait (RSL_{BeSt}). Our simulations assume that the modern sill depth of the Bering Strait (−53 m) has not substantially changed since 50 ka due to vertical displacement from processes unrelated to ice loading, such as longer term local tectonic, erosion, and sedimentation effects, as these are unlikely to be significant over the short time interval of our study (e.g., ref. (11)). We performed gravitationally self-consistent glacial isostatic adjustment simulations using three ice histories that encompass the range of MIS 3 GMSL estimates (Figs. 2*B* and 3*B*). The first ice history, ICE-5G (19), is characterized by MIS 3 GMSL values of −82 to −100 m (Fig. 3*B*). Peak predicted RSL_{BeSt} during mid-MIS 3 (50 to 35 ka) is −65 m, below the modern sill depth (−53 m, Fig. 3*C*). The second ice history is derived from a GMSL history constructed by scaling $\delta^{18}O$ records to coral reef sea-level records ((18); *Materials and Methods*) and is characterized by a GMSL of −71 to −62 m during mid-MIS 3. RSL_{BeSt} based on this ice history (18) predicts an exposed Bering Strait from 50 to 35 ka, with RSL_{BeSt} below or equal to the sill depth (−58 to −53 m) (Fig. 3*C*). In summary, neither of these ice volume reconstructions associated with canonical sea-level histories (18, 19) are consistent with our finding of a flooded Bering Strait during MIS 3.

Recent studies on the magnitude of GMSL during mid-MIS 3 (50 to 35 ka) suggest substantially higher peak GMSL compared with the previous reconstructions (22–24). We estimate RSL_{BeSt} for a set of ice histories consistent with these recent GMSL constraints. One important caveat to these alternative ice histories is that RSL_{BeSt} is sensitive to the nearby ice sheet history (specifically, the Cordilleran Ice Sheet (CIS)) (11, 30). The CIS extent during MIS 3 is poorly constrained by field data, representing a source of uncertainty (44) (*SI Appendix*, section S4). To address this, we simulate three cases of MIS 3 CIS geometry (large, intermediate, small; *SI Appendix*, section S4), each of which maintains the same ICE-PC-derived GMSL history (30). In all three simulations, the Bering Strait is flooded during MIS 3 until after ~34 ka (*SI Appendix*, Fig. S7). For the intermediate CIS history, RSL_{BeSt} is -11 to -20 m (yielding a water depth of 33 to 42 m; Fig. 3*C*) during mid-MIS 3. Our relative sea-level predictions suggest that a greater extent of the CIS results in a more deeply submerged Bering Strait (that is, a higher RSL_{BeSt}). Nevertheless, the three CIS geometries produce RSL_{BeSt} predictions that differ by less than 10 m (*Materials and Methods* and *SI Appendix*, Fig. S7). During MIS 3 and the LGM, glacial isostatic adjustment causes RSL_{BeSt} to be higher than GMSL by 20 to 30 m during MIS 3 and the LGM (compare Fig. 3 *B* and *C*). Nevertheless, our simulations show that GMSL changes are the dominant control on relative sea-level changes at the Bering Strait leading up to the LGM. Thus, a fully flooded Bering Strait during MIS 3 appears to require a global ice volume history in which MIS 3 ice volume is <50% (and in the case of ICE-PC, <30%) that of MIS 2 (22–24). This ice history contrasts with the long-dominant view of only modest ice retreat during MIS 3 (e.g., refs. (19–21)). A flooded Bering Strait before ~36 ka also requires that ice sheets grew quickly from MIS 3 until the LGM (Fig. 3*B*), consistent with previous findings (23, 45).

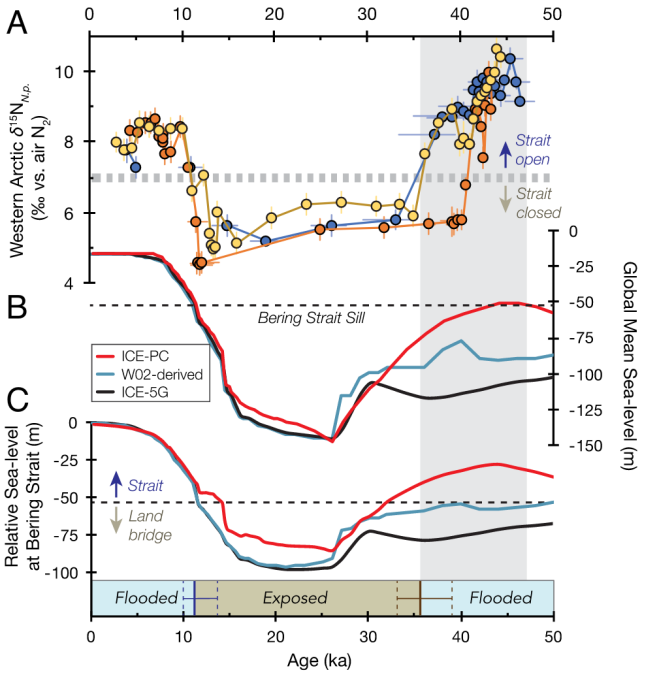

Fig. 3. Western Arctic Ocean $\delta^{15}N_{N.p.}$, global mean sea-level reconstructions, and glacial isostatic adjustment simulation of Bering Strait relative sea-level history. (*A*) Western Arctic Ocean $\delta^{15}N_{N.p.}$; dashed horizontal bar denotes maximum expected $\delta^{15}N_{N.p.}$ for an exposed Bering Strait (*Methods*). Vertical error bars denote the larger of measured or long-term replicate $\delta^{15}N_{N.p.}$ precision; horizontal error bars denote 68% quantiles (equivalent to ±1sd) of the age-depth model. (*B*) GMSL from ICE-5G (19) (black), from an ice history constructed from the pre-LGM GMSL in ref. (18) (W02-derived, blue), and from ICE-PC (red). (*C*) Relative sea level at the Bering Strait from ice volume histories in *B*, where ICE-PC RSL_{BeSt} is based on the intermediate Cordilleran Ice Sheet history (*Materials and Methods*). Black dashed line in *B* and *C* denotes modern sill depth of the Bering Strait (−53 m). Gray vertical shading denotes the timing of pre-LGM Bering Strait flooding reconstructed from panel (*A*). Colored bar at the bottom of *C* shows interpreted Bering Strait sea-level history. Brown vertical line denotes the reconstructed timing of Bering Strait closure in MIS 3; dashed brown lines are ±95% confidence intervals (this study). Blue vertical line and dashes denote the mean timing and range of observations for postglacial Bering Strait flooding, respectively (8, 11, 12).

Our Bering Strait submergence and GMSL reconstructions have implications for climate. First, relative sea level above −53 m at the Bering Strait until ~36 ka (Fig. 4*A*) supports recent estimates of peak MIS 3 GMSL near −40 m (22–24, 46, 47), indicating that peak MIS 3 global ice volumes were more similar to the Holocene than to the LGM (Fig. 4*B*). In contrast, global temperature proxies suggest that MIS 3 was notably colder than the Holocene and only slightly warmer than the LGM (Fig. 4*D*). If global temperatures during MIS 3 were indeed similar to the LGM, why was ice volume so much lower during MIS 3? The growth of ice volume in late MIS 3 might reflect nonlinearity in the sensitivity of ice volume to CO_2 radiative forcing (Fig. 4*E*), with ice volume responding more to CO_2 change when CO_2 is low and climate is cold (48). However, such nonlinearity would need to be very strong to explain the observations, with the radiative forcing from the decline in atmospheric CO_2 from 220 to 190 ppmv between 40 and 30 ka driving >60 m sea-level equivalent ice volume growth (Fig. 4 *B* and *E*). An alternative possibility is that Northern Hemisphere ice volume growth was more directly controlled by peak summer insolation than by global temperature (13, 24, 49), as supported by the coincidence of declining 65°N summer insolation (Fig. 4*C*) and increasing ice volume through late MIS 3 (Fig. 4*B*) despite relatively little global cooling (Fig. 4*D*). This distinction may indicate a strong role for local summer insolation in driving ice loss (Fig. 4 *B* and *C*), for example, by direct irradiance-driven ablation (e.g., ref. (50)) or as a local driver

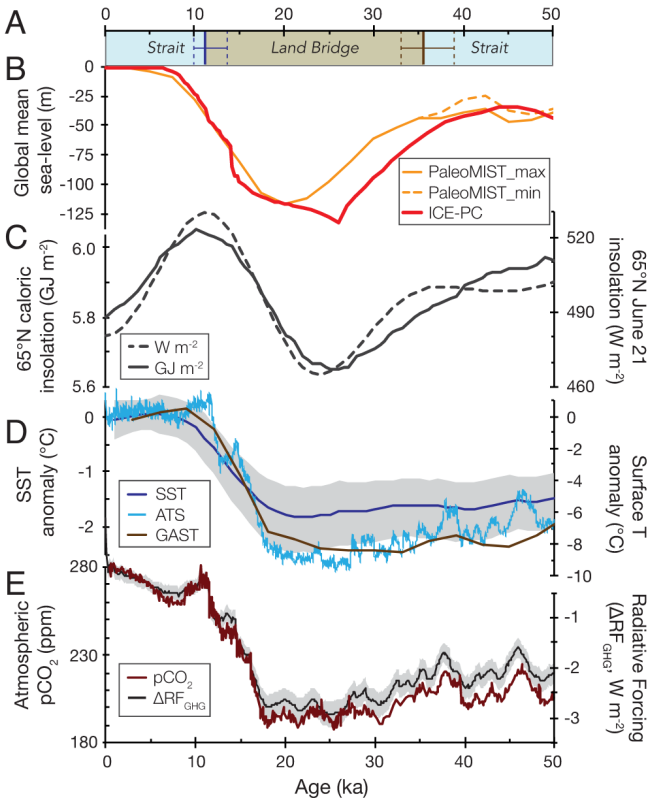

Fig. 4. Comparison of histories of Bering Strait flooding, sea level, climate, and climate forcings over the last 50 kyr. (*A*) Bering Strait and Bering Land Bridge intervals based on western Arctic $\delta^{15}N_{N.p.}$ (as in Fig. 3); (*B*) ICE-PC (this study, red) and PaleoMIST ((24), orange) sea-level reconstructions. (*C*) 65°N summer solstice mean daily insolation (dashed, W m^{-2}) and caloric summer half-year insolation (51) (solid, GJ m^{-2}). (*D*) Global average surface temperature anomaly (52) (brown), Antarctic ice core temperature stack (ATS) anomaly (53) (cyan), and global sea surface temperature (SST) anomaly (49) (blue, shading is 95% CI). (*E*) Atmospheric CO_2 concentration (54, 55) (dark red) and cumulative greenhouse gas (CO_2, CH_4, and N_2O) radiative forcing (56) (ΔRF_{GHG}; black, shading is ±1sd).

of summertime air temperature change over the Northern Hemisphere ice sheets.

Second, given the importance of ice albedo to global temperature, a complementary question emerges: If ice volume during MIS 3 was sufficiently low to allow for a flooded Bering Strait, then why was MIS 3 so cold? One possibility is that the radiative impact of low ice volume was compensated by spatially extensive but thin land ice and snow cover as well as sea ice during MIS 3 (49). The cold MIS 3 climate could also indicate an outsized importance of low atmospheric CO_2 concentrations during MIS 3 (200 to 220 ppmv, Fig. 4*E*) to Earth's radiative balance (49). In general, the deviation from linear correlation between climate and ice volume during MIS 3 provides a new test for models of climate and glaciation. Extending the use of the Bering Strait as a sea-level gauge further back in time will likely offer additional constraints on the mechanisms underlying the glacial cycles as glaciological and climatic phenomena.

Third, in both simple and fully coupled climate models, the Bering Strait's sea-level history contributes to the response of North Atlantic Deep Water production to regional freshwater perturbations (5, 6). These simulations led to the proposal that subaerial exposure of the Bering Strait was a prerequisite for the millennial-scale Northern hemisphere climate variability during the last glacial period (5, 6). However, our data indicate that millennial-scale variability in climate and ocean circulation occurred both when the Bering Strait was flooded (46 to 36 ka) and exposed (36 to 11.5 ka) (Fig. 2). Thus, closure of the Bering Strait was not needed for the occurrence of millennial-scale variability during the last ice age.

Finally, our reconstructed Bering Strait submergence history has implications for humans' arrival in the Americas. Recent evidence for human presence in North America between 23 and 21 ka (15) appears to require that humans migrated across Beringia before the onset of LGM conditions (15, 16). Limited regional archaeological records of human occupation before and during the LGM, particularly from eastern Beringia, preclude identification of the key factors controlling human migration at this time. However, comparison of our results with demographic age modeling of Beringian populations suggests one possibility. Humans were present in North Siberia as early as 45 ka (57), with a unique Ancient North Siberian population diverging from East Asians by 39 ka (95% CI 45.8 to 32.2 ka, ref. (58)). A second distinct Ancient Beringian population with direct ancestry to Native Americans emerged from East Asians at 36 ± 1.5 ka (16). Our data indicate that Siberia and Alaska were separated by the Bering Strait until the Bering Land Bridge formed at $35.7^{+3.3}_{-2.4}$ ka. Together, these findings suggest that, in the context of the last ~50 kyr, humans migrated into the Americas as soon as the Bering Land Bridge allowed for their passage. If correct, such simultaneity implies a strong drive for migration among the ice-age human populations in Siberia.

Materials and Methods

Three western Arctic cores were obtained from Mendeleev Ridge: Site B8 (78.13°N, 176.74°W, 1,031 m water depth), Site B12 (79.99°N, 174.29°W, 1,609 m water depth), and Site B17 (81.27°N, 178.97°E, 2,217 m water depth). The central Arctic core, Site B28, was obtained from Lomonosov Ridge (88.87°N, 140.18°E, 1,990 m water depth). Sediment samples were taken every 1 cm. Approximately 1,500 *Neogloboquadrina pachyderma* sinistral (Ehrenberg) tests (5 to 7 mg) were picked from the 150 to 300 μm size fraction under a binocular microscope. Foraminifera-bound nitrogen isotope analyses were performed at Princeton University following the procedures described in ref. (8), which are modified from refs. (59) and (60). Briefly, *N. pachyderma* samples were gently crushed; subjected to clay removal, reductive cleaning, and oxidative cleaning; dissolved in 4 N HCl to release bound organic nitrogen; oxidized to nitrate with basic potassium persulfate; and converted to N_2O gas via the denitrifier method (61). N isotopes were measured on N_2O with a custom-built, automated, helium continuous flow-based extraction and purification system coupled to a MAT253 isotope ratio mass spectrometer (62–64). The analytical precision based on long-term replication of internal carbonate-bound organic N standards is <±0.30‰ (1sd). The analytical precision of full procedural replicate $\delta^{15}N_{N.p.}$ analyses averaged ±0.22‰ (1sd, n = 42; error bars plotted on Figs. 2*D* and 3*A*). Further information on sediment core age models, constraints on the isotopic composition of nitrate in the polar Northern Hemisphere (Fig. 1*A*), and the interpretation of Bering Strait sea-level history from $\delta^{15}N_{N.p.}$ is provided in the *SI Appendix*, Texts S1–S3.

The growth and decay of ice sheets produces a complex sea-level change pattern as the solid Earth responds through crustal deformation, perturbations to the Earth's gravitational field, and changes to the Earth's rotation axis. Our gravitationally self-consistent sea-level calculations are based on the theory and pseudo-spectral algorithm of (65) with a spherical harmonic truncation at degree and order 256. These calculations include the impact of load-induced Earth rotation changes on sea level (66, 67), evolving shorelines, and the migration of grounded, marine-based ice (65, 68–70). Our numerical predictions require models for Earth's viscoelastic structure and the history of global ice cover. We use an Earth model characterized by a lithospheric thickness of 48 km, and an upper and lower mantle viscosity of 0.5 × 10^{21} Pa s and 5 × 10^{21} Pa s, respectively (as in ref. (11)). An evaluation of these results using an alternative Earth model (VM2) is provided in the *SI Appendix*, Text S4.

Our relative sea-level predictions for the Bering Strait additionally require global ice sheet histories to be input into the Earth model described above.

Here, we employ three ice sheet histories: ICE-5G, ICE-PC, and W02-derived (*SI Appendix*, Table S1). The ICE-5G ice history is from ref. (19). The ICE-PC ice history is from ref. (23) and is constrained such that the LGM and deglaciation (26 ka to 0 ka) global mean sea-level history is identical to the ICE-6G ice history (71), while the pre-LGM ice history is scaled to fit a global mean sea-level (GMSL) history based on fitting GMSL highstand constraints during MIS 3, MIS 5a, and MIS 5c (23). The W02-derived ice history is a global ice sheet history for which the deglacial ice sheet history is identical to the ICE-5G deglacial history (26 ka to 0 ka, ref. 15), while the glaciation phase (before 26 ka) adopts ice geometries based on Waelbroeck et al.'s GMSL history (18). Before 26 ka, the ice history at each time point is set by the GMSL history in ref. (18), with ice geometry assumed to be identical to the post-LGM ICE-5G ice history in the period with the same GMSL value. We note that the resultant GMSL history of the W02-derived ice history (Fig. 3*B*) is not identical to the originally published GMSL history of ref. (18). The Earth model is run using these three ice histories at 1 to 2 kyr timesteps.

Because the melt and growth history of the proximal Cordilleran Ice Sheet (CIS), and especially its rapid collapse events, can have a first-order effect on Bering Strait relative sea level (11), it is also essential to consider possible CIS geometries in modeling Bering Strait relative sea level. To address the sensitivity of Bering Strait relative sea level to the CIS, we test a suite of CIS ice sheet geometries, which incorporate what we term a small, intermediate, and large CIS. We produce a set of three ice histories corresponding to the ICE-PC GMSL history, which itself is based on the ICE-6G deglaciation history (71) (Fig. 3*B* and *SI Appendix*, Table S1). For the intermediate CIS (ICE-PC, Fig. 3*C*), the ice history's geographic distribution assumes that CIS ice geometry prior to 26 ka is identical to post-26 ka ice geometry for the same GMSL value based on ICE-6G deglaciation history (71). In contrast, for the large CIS (ICE-PC2), prior to 26 ka, the CIS maintains the same boundary as it had during the LGM, with its ice thickness scaled to fit the ICE-PC GMSL history (*SI Appendix*, Fig. S7). This large CIS, characterized by maximum ice extent, is part of a North American Ice Sheet history with a reduced MIS 3 eastern Laurentide Ice Sheet (23). For the small CIS (ICE-MIST), we adopt the CIS history (defined as west of 120° W, from 80 to 26 ka) from PaleoMIST (24). Each of these ice histories is characterized by an identical GMSL history (ICE-PC in Fig. 3*B*) that is maintained by changing ice thickness over Scandinavia and Antarctica, locations that are far-field to our site of interest at the Bering Strait. For the intermediate and large CIS history (ICE-PC and ICE-PC2), the deglaciation history (26 to 0 ka) is adopted from the GI-31 ice history (11, 30), and incorporates substantial melting of the North American ice sheet saddle, which connected the Cordilleran and Laurentide Ice Sheets, from 13 to 11.5 ka (*SI Appendix*, Table S1).

Data, Materials, and Software Availability. Foraminifera-bound N isotopes, sediment core age models, and sea level simulations data are included in the *SI Appendix*, Dataset S1.

ACKNOWLEDGMENTS. We thank Sergey Oleynik and Laura Gemery for laboratory assistance and Peter Huybers for discussions. J.R.F., D.M.S., and O.M.U. were supported by NSF OCE-2054780; J.R.F. was also supported by the Max Planck Society (with A.M.-G. and G.H.H.) and by the Tuttle Fund of the Department of Geosciences, Princeton University (with D.M.S.). T.P. was supported by NSF OCE-2054757. T.M.C. was funded by the United States Geological Survey Climate Research and Development Program. Any use of trade, firm, or product names is for descriptive purposes only and does not imply endorsement by the United States Government.

Author affiliations: [a]Department of Geosciences, Princeton University, Princeton, NJ 08544; [b]Max Planck Institute for Chemistry, Mainz 55128, Germany; [c]Earth and Planetary Sciences, University of California-Santa Cruz, Santa Cruz, CA 95064; [d]Department of Earth and Planetary Sciences, Harvard University, Cambridge, MA 02138; [e]Department of Marine Sciences, University of Connecticut, Groton, CT 06340; [f]Florence Bascom Geoscience Center, United States Geological Survey, Reston, VA 20192; [g]Department of Geosciences, Environment and Society, Université Libre de Bruxelles, Brussels 1050, Belgium; and [h]Department of Earth Sciences, ETH Zürich, Zürich 8092, Switzerland

1. S. L. Danielson *et al.*, Sounding the Northern Seas. *EOS* **96** (2015), 10.1029/2015EO040975.
2. R. A. Woodgate, Increases in the Pacific inflow to the Arctic from 1990 to 2015, and insights into seasonal trends and driving mechanisms from year-round Bering Strait mooring data. *Prog. Oceanogr.* **160**, 124–154 (2018).
3. A. Jahn, M. M. Holland, Implications of Arctic sea ice changes for North Atlantic deep convection and the meridional overturning circulation in CCSM4-CMIP5 simulations. *Geophs. Res. Lett.* **40**, 1206–1211 (2013).
4. M. Yamamoto-Kawai, E. Carmack, F. McLaughlin, Nitrogen balance and Arctic throughflow. *Nature* **443**, 43 (2006).
5. A. M. De Boer, D. Nof, The Bering Strait's grip on the northern hemisphere climate. *Deep Sea Res. Pt.* **51**, 1347–1366 (2004).
6. A. Hu *et al.*, Role of the Bering Strait on the hysteresis of the ocean conveyor belt circulation and glacial climate stability. *Proc. Natl. Acad. Sci. U.S.A.* **109**, 6417–6422 (2012).
7. S. K. Lauvset *et al.*, A new global interior ocean mapped climatology: The 1° x 1° GLODAP version 2. *Earth Syst. Sci. Data* **8**, 325–340 (2016), 10.5194/essd-8-325-2016.
8. J. R. Farmer *et al.*, Arctic Ocean stratification set by sea level and freshwater inputs since the last ice age. *Nat. Geosci.* **14**, 684–689 (2021), 10.1038/s41561-021-00789-y.
9. F. McLaughlin, E. Carmack, R. Macdonald, A. J. Weaver, J. Smith, The Canada Basin, 1989:1995: Upstream events and far-field effects of the Barents Sea. *J. Geophys. Res.* **107**, 3082 (2002).
10. S. L. Danielson *et al.*, Coupled wind-forced controls of the Bering-Chukchi shelf circulation and the Bering Strait throughflow: Ekman transport, continental shelf waves, and variations of the Pacific-Arctic sea surface height gradient. *Prog. Oceanogr.* **125**, 40–61 (2014).
11. T. Pico, J. X. Mitrovica, A. C. Mix, Sea level fingerprinting of the Bering Strait flooding history detects the source of the Younger Dryas climate event. *Sci. Adv.* **6**, eaay2935 (2020).
12. M. Jakobsson *et al.*, Post-glacial flooding of the Bering Land Bridge dated to 11 cal ka BP based on new geophysical and sediment records. *Clim. Past.* **13**, 991–1005 (2017), 10.5194/cp-13-991-2017.
13. P. U. Clark *et al.*, The last glacial maximum. *Science* **325**, 710–714 (1959).
14. D. M. Hopkins, Cenozoic history of the Bering land bridge. *Science* **129**, 1519–1528 (1959).
15. M. R. Bennett *et al.*, Evidence of humans in North America during the Last Glacial Maximum. *Science* **373**, 1528–1531. 10.1126/science.abg7586 (2021).
16. J. V. Moreno-Mayar *et al.*, Terminal Pleistocene Alaskan genome reveals first founding population of native Americans. *Nature* **553**, 203–207 (2018).
17. D. M. Hopkins, Sea level history in Beringia during the past 250,000 years. *Quat. Res.* **3**, 520–540 (1973).
18. C. Waelbroeck, L. Labeyrie, E. Michel, J. C. Duplessy, J. F. McManus, Sea-level and deep water temperature changes derived from benthic foraminifera isotopic records. *Quat. Sci. Rev.* **21**, 295–305 (2002).
19. W. R. Peltier, R. G. Fairbanks, Global glacial ice volume and last glacial maximum duration from an extended Barbados sea level record. *Quat. Sci. Rev.* **25**, 3322–3337 (2006).
20. K. M. Grant *et al.*, Rapid coupling between ice volume and polar temperature over the past 150,000 years. *Nature* **491**, 744–747 (2012), 10.1038/nature11593.
21. R. M. Spratt, L. E. Lisiecki, A late Pleistocene sea level stack. *Clim. Past* **12**, 1079–1092 (2016), 10.5194/cp-12-1079-2016.
22. T. Pico, J. X. Mitrovica, K. L. Ferrier, J. Braun, Global ice volume during MIS 3 inferred from a sea-level analysis of sedimentary core records in the Yellow River Delta. *Quat. Sci. Rev.* **152**, 72–79 (2016).
23. T. Pico, J. R. Creveling, J. X. Mitrovica, Sea-level records from the US mid-Atlantic constrain Laurentide ice sheet extend during marine isotope stage 3. *Nat. Commun.* **8**, 15612 (2017).
24. E. J. Gowan *et al.*, A new global ice sheet reconstruction for the past 80,000 years. *Nat. Commun.* **12**, 1199 (2021), 10.1038/s41467-021-21469-w.
25. P. Fretwell *et al.*, Bedmap2: Improved ice bed, surface and thickness datasets for Antarctica. *The Cryosphere* **7**, 375–393 (2013), 10.5194/tc-7-375-2013.
26. C. R. Stokes *et al.*, On the reconstruction of palaeo-ice sheets: Recent advances and future challenges. *Quat. Sci. Rev.* **125**, 15–49 (2015).
27. F. D. Hibbert *et al.*, Coral indicators of past sea-level change: A global repository of U-series dated benchmarks. *Quat. Sci. Rev.* **145**, 1–56 (2016).
28. de Gelder, G., Husson, L., Pastier, A.-M., Fernández-Blanco, D., Pico, T., Chauveau, D., Authemayou, C., & Pedoja, K. (2022). High interstadial sea levels over the past 420ka from the Huon Peninsula, Papua New Guinea. *Communications Earth & Environment*, **3**. https://doi.org/10.1038/s43247-022-00583-7
29. North Greenland Ice Core Project Members, High-resolution record of Northern hemisphere climate extending into the last interglacial period. *Nature* **431**, 147–151 (2004).
30. T. Pico, A. Robel, E. Powell, A. C. Mix, J. X. Mitrovica, Leveraging the Rapid Retreat of the Amundsen Gulf Ice Stream 13,000 Years Ago to Reveal Insight Into North American Deglaciation. *Geophys. Res. Let.* **46**, 12101–12107 (2019), 10.1029/2019GL084789.
31. L. E. Lisiecki, J. V. Stern, Regional and global benthic $d^{18}O$ stacks for the last glacial cycle. *Paleoceanography* **31**, 1368–1394 (2016).
32. Lehmann, M. F., Sigman, D. M., McCorkle, D. C., Brunelle, B. G., Hoffmann, S., Kienast, M., Cane, G., & Clement, J. (2005). Origin of the deep Bering Sea nitrate deficit: Constraints from the nitrogen and oxygen isotopic composition of water column nitrate and benthic nitrate fluxes. *Global Biogeochemical Cycles*, **19**(4), https://doi.org/10.1029/2005gb002508
33. J. Granger *et al.*, Coupled nitrification-denitrification in sediment of the eastern Bering Sea shelf leads to ^{15}N enrichment of fixed N in shelf waters. *J. Geophys. Res.* **116**, C11006 (2011).
34. J. Granger, D. M. Sigman, J. G. Gagnon, J.-E. Tremblay, A. Mucci, On the properties of the Arctic halocline and deep water masses of the Canada Basin from nitrate isotope ratios. *J. Gephys. Res. Oceans* **123**, 5443–5458 (2018).
35. F. Fripiat *et al.*, Influence of the bordering shelves on nutrient distribution in the Arctic halocline inferred from water column nitrate isotopes. *Limnol. Oceanogr.* **63**, 2154–2170 (2018).
36. Z. W. Brown, K. L. Casciotti, R. S. Pickart, J. H. Swift, K. R. Arrigo, Aspects of the marine nitrogen cycle of the Chukchi Sea shelf and Canada Basin. *Deep Sea Res. Pt.* **118**, 73–87 (2015).
37. H. Ren, D. M. Sigman, R. C. Thunell, M. G. Prokopenko, Nitrogen isotopic composition of planktonic foraminifera from the modern ocean and recent sediments. *Limnology and Oceanography*, **57**, 1011–1024 (2012). 10.4319/lo.2012.57.4.1011.
38. M. A. Altabet, R. Francois, Sedimentary nitrogen isotopic ratio as a recorder for surface ocean nitrate utilization. *Glob. Biogeochem. Cy.* **8**, 103–116 (1994).
39. A. Randelhoff *et al.*, Pan-Arctic Ocean primary production constrained by turbulent nitrate fluxes. *Front. Mar. Sci.* **7**, 150 (2020), 10.3389/fmars.2020.00150.
40. J. W. McClelland *et al.*, Particulate organic carbon and nitrogen export from major Arctic rivers. *Glob. Biogeochem. Cy.* **30**, 629–643 (2016), 10.1002/2015GB005351.
41. B. Thibodeau, D. Bauch, M. Voss, Nitrogen dynamic in Eurasian coastal Arctic ecosystem: Insight from nitrogen isotope. *Glob. Biogeochem. Cy.* **31**, 836–849 (2017).

42. M. Straub *et al.*, Changes in North Atlantic nitrogen fixation controlled by ocean circulation. *Nature* **501**, 200–203 (2013), 10.1038/nature12397.
43. B. G. Brunelle *et al.*, Evidence from diatom-bound nitrogen isotopes for subarctic Pacific stratification during the last ice age and a link to North Pacific denitrification changes. *Paleoceanography* **22**, PA1215 (2007).
44. J. Seguinot, I. Rogozhina, A. P. Stroeven, M. Margold, J. Kleman, Numerical simulations of the Cordilleran ice sheet through the last glacial cycle. *The Cryosphere* **10**, 639–664 (2016).
45. K. Lambeck, H. Rouby, A. Purcell, Y. Sun, M. Sambridge, Sea level and global ice volumes from the Last Glacial maximum to the holocene. *Proc. Natl. Acad. Sci. U.S.A.* **111**, 15296–15303 (2014), 10.1073/pnas.1411762111.
46. A. S. Dalton *et al.*, Was the Laurentide ice sheet significantly reduced during marine isotope stage 3? *Geology* **47**, 111–114 (2019), 10.1130/G45335.1.
47. C. L. Batchelor *et al.*, The configuration of Northern hemisphere ice sheets through the quaternary. *Nat. Commun.* **10**, 3713 (2019), 10.1038/s41467-019-11601-2.
48. P. Liautaud, P. Huybers, Increased sea level sensitivity to CO_2 forcing across the middle pleistocene transition from ice-albedo and ice-volume nonlinearities. *J. Clim.* **34**, 9693–9708 (2021), 10.1175/jcli-d-21-0192.1.
49. J. D. Shakun, D. W. Lea, L. E. Lisiecki, M. E. Raymo, An 800-kyr record of global surface ocean $\delta^{18}O$ and implications for ice volume-temperature coupling. *Earth Planet. Sci. Lett.* **426**, 58–68 (2015).
50. M. Suwa, M. L. Bender, Chronology of the Vostok ice core constrained by O_2/N_2 ratios of occluded air, and its implication for the Vostok climate records. *Quat. Sci. Rev.* **27**, 1093–1106 (2008).
51. P. C. Tzedakis, M. Crucifix, T. Mitsui, E. W. Wolff, A simple rule to determine which insolation cycles lead to interglacials. *Nature* **542**, 427–432 (2017), 10.1038/nature21364.
52. C. W. Snyder, Evolution of global temperature over the past two million years. *Nature* **538**, 226–228 (2016), 10.1038/nature19798.
53. F. Parrenin *et al.*, Synchronous change of atmospheric CO_2 and Antarctic temperature during the last deglacial warming. *Science* **339**, 1060–1063 (2013), 10.1126/science.1226368.
54. E. Monnin *et al.*, Evidence for substantial accumulation rate variability in Antarctica during the Holocene, through synchronization of CO_2 in the Taylor Dome, Dome C and DML ice cores. *Earth Planet. Sci. Lett.* **224**, 45–54 (2004).
55. T. K. Bauska, S. A. Marcott, E. J. Brook, Abrupt changes in the global carbon cycle during the last glacial period. *Nat. Geosci.* **14**, 91–96 (2021).
56. P. Köhler, C. Nehrbass-Ahles, J. Schmitt, T. F. Stocker, H. Fischer, A 156 kyr smoothed history of the atmospheric greenhouse gases CO_2, CH_4, and N_2O and their radiative forcing. *Earth Syst. Sci. Data* **9**, 363–387 (2017), 10.5194/essd-9-363-2017.
57. V. V. Pitulko *et al.*, Early human presence in the Arctic: Evidence from 45,000-year-old mammoth remains. *Science* **351**, 260–263 (2016), 10.1126/science.aad0554.
58. M. Sikora *et al.*, The population history of northeastern Siberia since the Pleistocene. *Nature* **570**, 182–188 (2019), 10.1038/s41586-019-1279-z.
59. A. N. Knapp, D. M. Sigman, F. Lipschultz, N isotopic composition of dissolved organic nitrogen and nitrate at the Bermuda Atlantic time-series study site. *Global Biogeochem. Cycles* **19**, GB1018 (2005).
60. H. Ren *et al.*, Foraminiferal isotope evidence of reduced nitrogen fixation in the ice age Atlantic Ocean. *Science* **323**, 244–248 (2009).
61. D. M. Sigman *et al.*, A bacterial method for the nitrogen isotopic analysis of nitrate in seawater and freshwater. *Anal. Chem.* **73**, 4145–4153 (2001).
62. K. L. Casciotti, D. M. Sigman, M. G. Hastings, J. K. Böhlke, A. Hilkert, Measurement of the oxygen isotopic composition of nitrate and seawater and freshwater using the denitrifier method. *Anal. Chem.* **74**, 4905–4912 (2002).
63. M. R. McIlvin, K. L. Casciotti, Technical updates to the bacterial method for nitrate isotopic analyses. *Anal. Chem.* **83**, 1850–1856 (2011).
64. M. A. Weigand, J. Foriel, B. Barnett, S. Oleynik, D. M. Sigman, Updates to instrumentation and protocols for isotopic analysis of nitrate by the denitrifier method. *Rapid Commun. Mass Spectrom.* **30**, 1365–1383 (2016).
65. R. A. Kendall, J. X. Mitrovica, G. A. Milne, On post-glacial sea level – II. Numerical formulation and comparative results on spherically symmetric models. *Geophys. J. Int.* **161**, 679–706 (2005), 10.1111/j.1365-246X.2005.02553.x.
66. G. Milne, J. X. Mitrovica, Postglacial sea-level change on a rotating Earth: First results from a gravitationally self-consistent sea-level equation. *Geophys. J. Int.* **126**, F13–F20 (1996).
67. J. X. Mitrovica, J. Wahr, I. Matsuyama, A. Paulson, The rotational stability of an ice-age earth. *Geophys. J. Int.* **161**, 491–506 (2005).
68. P. Johnston, The effect of spatially non-uniform water loads on prediction of sea-level change. *Geophys. J. Int.* **114**, 615–634 (1993).
69. K. Lambeck, A. Purcell, P. Johnston, M. Nakada, Y. Yokoyama, Water-load definition in the glacio-hydro-isostatic sea-level equation. *Quat. Sci. Rev.* **22**, 309–318 (2003).
70. G. A. Milne, J. X. Mitrovica, J. L. Davis, Near-field hydro-isostasy: The implementation of a revised sea-level equation. *Geophys. J. Int.* **139**, 462–482 (1999).
71. W. R. Peltier, D. F. Argus, R. Drummond, Space geodesy constrains ice age terminal deglaciation: The global ICE-6G_C (VM5a) model. *J. Gephys. Res. Solid Earth* **120**, 450–487 (2015), 10.1002/2014JB011176.